Effects of temperature and nanofluid type on the oil recovery from a vertical porous media in antigravity fluid injection

Naser Asadzadeh[1], Majid Ahmadlouydarab*[1], and Amin Sharifi Haddad[2]

[1]Faculty of Chemical & Petroleum Engineering, University of Tabriz, Iran
[2]School of Engineering, King's College, University of Aberdeen, Aberdeen AB24 3UE, United Kingdom
*Corresponding author: mahmadlouydarab@tabrizu.ac.ir

Abstract:

Recent researches indicate that the injection of nanofluid solutions into oil reservoirs enhances oil recovery, but the impact of key important parameters such as antigravity fluid injection has not yet been well understood. In current experimental investigation, effects of temperature and antigravity injection on the enhancement of oil recovery was studied. Additionally, effects of wettability alteration, interfacial tension, and viscosity were investigated. Pure water, TiO_2, CuO, and γ-Al_2O_3 nanofluids were considered as injected fluid. During the antigravity fluid injection process, decreasing the capillary number enhanced the oil recovery. This increment for pure water, TiO_2, CuO, and γ-Al_2O_3 nanofluids injection was 42.8, 65.7, 73.5, and 75.7%, respectively. Compared to the gravity-aligned injection, these results show enhancement by up to 18.25, 19.7, 17.5, and 23.7%. Moreover, for injection in antigravity direction when water, TiO_2, CuO, and γ-Al_2O_3 nanofluids injected at 90°C oil recovery enhanced by 7.8, 5.2, 3.7, and 2.75%, respectively, compared to the results obtained for injection at 25°C. Besides, oil recovery enhanced substantially by interfacial tension reduction when using nanofluids instead of water. For instance, the maximum recovery belongs to γ-Al_2O_3 nanofluid by 43.5% as the interfacial tension reduced from 45.03 mN/m for oil-water to 2.36 mN/m for oil and γ-Al_2O_3 nanofluid. Furthermore, increasing the injection temperature from 25 °C to 90 °C reduced the interfacial tension. This reduction for water injection was 15.8%, and 21.2% for γ-Al_2O_3 nanofluid injection.

Keywords: Enhanced Oil Recovery; Hot nanofluids; antigravity injection; Temperature; Interfacial tension reduction; Vertical porous medium

1. Introduction

It is crucial to select an appropriate enhanced oil recovery method in the modern era due to the urgent demand for oil and its products [1]. Basically, oil recovery from reservoirs is divided into three phases: primary, secondary, and tertiary exploitation [2]. Because of the high pressure in the reservoir, the preliminary exploitation is carried out using existing natural driving mechanisms, including thrust energy or rock-fluid expansion [3]. Given the relatively weak natural displacements, secondary production processes like gas injection, water flooding, or alternate water and gas injection are used after decreasing the initial exploitation. Since only 30% to 50% of the oil in the reservoirs can be recovered using primary and secondary methods, tertiary exploitation techniques, also known as enhanced oil recovery, are employed to boost oil generation from the reservoirs [4]. Generally, the best way to deal with the issue of declining production and reservoir longevity is to enhance oil recovery. It is important to note that the primary and secondary recovery methods goals are to increase the oil mobility in the reservoir. Of course, because of capillary force and adhesion, oil cannot be fully recovered [5, 6]. Generally, injection of miscible solvents, carbon dioxide, flooding of polymer and surfactant, and thermal techniques have contributed to oil recovery. Moreover, the nanofluid injection is an interesting method. Numerous investigations have demonstrated that incorporating nanoparticles into a fluid via flooding can alter the interfacial tension of oil/water phases [7] and wettability [8-13] as well as augment their characteristics [14, 15]. Indeed, nanoparticles enhance oil recovery and regulate the mobility ratio [16, 17]. The majority of the established chemical methods reduce permeability after injection, and by accumulating within the reservoir rock, they obstruct the reservoir rock's pores. As a result, nanoparticles have effective applications in oil recovery processes for a variety of reasons. These reasons include the size smallness, which facilitates the easy entry into reservoir rock pores and recover oil without entrapment, the capacity to stabilize emulsions, establish an appropriate dynamic ratio, altering the properties of the base fluid, environmentally friendly, and high temperature and pressure tolerance. In recent decades, large numbers of studies have focused on the nanoparticles applicability in enhancing oil recovery. For example, altering wettability of carbonate reservoirs were studied by Hamouda & Gomari [18]. They examined the impact of temperature on the contact angle, interfacial tension, and zeta potential parameters. They discovered that variations in contact angle at high temperatures are comparable to variations in interfacial tension. The contact angle was reduced from 160° to 68° at elevated temperatures. This trend

demonstrated that as carbonate reservoir temperatures rise, the reservoirs shift from petrophilic to hydrophilic. Also, they came to the conclusion that there is potential for a critical temperature for the highest wettability alterations. No further wettability alteration will take place if the temperature rises above this point.

Later, Suleimanov and coworkers [19] employed nanofluids for enhancing oil recovery purpose in a laboratory scale. They conducted their research using an aqueous solution made up of anionic surfactants and non-ferrous metal nanoparticles. When compared to the water solution surface, the application of nanofluids decreased interfacial tension at the oil boundary by 70-90%.

Maghzi and his colleagues [20, 21] examined the impact of silica and polyacrylamide nanoparticles on enhanced oil recovery using chemical and laser micromodels. They finally concluded that the silica nanoparticles caused enhanced oil recovery during polymer flooding.

El-Diasty and Aly [22] presented novel ways to use nanotechnology for enhancing oil recovery in old fields. Researchers highlighted the possibility of using nanoparticles for enhancing oil recovery, as well as nanoparticles small size in comparison to the porous pores. The findings demonstrated that, without affecting permeability, nanoparticles could move freely in porous rocks.

According to a research conducted by Yousefvand et al. [23], the silica nanoparticles adsorption on the cavity wall and bottlenecks leads to strong hydrophilicity in micromodel cavities and makes hydrolyzed polyacrylamide perform better in oil recovery.

In another experimental study, Roustaei and Bagherzadeh [24] investigated enhanced oil recovery in carbonate reservoirs employing silicon oxide nanoparticles. To calculate the optimal nanofluid concentration value for injection into carbonate core specimens, they examined the impact of nanoparticle concentration on wettability and interfacial tension.

To assess the improvement of foam stability in porous media employing nanoparticles, Wang et al. [25] used the best foam formulation (surfactant and polymer) in various salinities. Air injection was used to examine the one-dimensional flow of the foam produced in the testing environment. The pressure declines in rock fractures in the availability of nanoparticles, the fluid injection discharge on the foam in the porous medium, and the foam in the presence and absence of carbon nanotubes were also all studied.

Later, Soleimani et al. [26] synthesized zinc oxide nanoparticles on an experimental scale to decrease oil-water interfacial tension in favor of enhanced oil recovery. Enhanced oil recovery resulted from zinc oxide's adsorption on the rock's surface due to wettability and a decrease in capillary force. The nanofluid was afterward synthesized by varying the concentration of zinc oxide nanoparticles to achieve the favored value in the interfacial tension test (employing the hanging drop method).

The effect of temperature on the stability of nanoparticle/surfactant solutions and oil recovery as well as the simultaneous and mutual effects of parameters were investigated by Mahmoudi et al. [27]. Their results showed that the concentration of nanoparticles is the most important factor affecting the stability of the solution, which leads to the improvement of oil recovery.

Furthermore, some of the factors influencing interfacial tension and wettability variations in the recovery of remaining oil trapped in reservoirs have been studied [28]. The findings demonstrate that various wettability characteristics enhance oil recovery only by interfacial tension reduction, and the impact of wettability alterations can differ because of various states of preliminary wettability.

Chandio et al. [29] conducted an empirical assessment of the effects of concentration, salinity, and the mechanisms of enhanced oil recovery using hydrophilic silica nanofluid. The results indicated the optimal concentration of 0.05 %wt in elevated salinities with the greatest potential for recovery, wettability alteration, and interfacial tension reduction.

Recently, in a research conducted in 2022, in order to enhance oil recovery, an innovative nanofluid based on polyoxyethylated graphene oxide has been prepared [30]. The findings of the study suggested that the produced nanofluid has the potential to enhance oil recovery.

Another significant point is the effect of gravity in vertical displacements in porous media. Four factors control the efficiency of vertical sweep which including; density, mobility ratio, difference between vertical and horizontal permeability and capillary forces. Upward injection of fluids against gravity improves sweep efficiency and enhance oil recovery by reducing viscous fingering. A major aim of using vertical injection wells is that they may already be available from previous production [31]. On the other hand, the importance of vertical injection compared to horizontal injection has been shown in reducing drilling costs [32].

The effect of vertical downward, vertical upward and horizontal injection mode on oil recovery has been studied [33]. The results demonstrated that the strategy of gas injection vertically downwards is the most efficient method among the three injection modes. Additionally, vertical injection and horizontal production systems have been shown to provide faster and more oil recovery compared to horizontal injection and production well systems [34]. Alkaline/surfactant/polymer (ASP) injection aimed at enhancing oil recovery in a physical model of a vertical heterogeneous reservoir not only displaces residual oil in high-permeability reservoirs, but also showed that displaces the residual oil in the low-and medium-permeability layers by increasing the displacement volume and displacement efficiency [35].

Overall, literature review shows that effects of crucial factors, including the effect of anti-gravity fluid injection on the oil recovery enhancement in the porous medium, has not yet been understood. So, in current study to enhance the current knowledge, effects of anti-gravity hot/cold nanofluid injection on the oil recovery from a model porous medium will be studied.

2. Materials and methods

2.1. Materials

Nanoparticles, such as titanium dioxide (TiO_2), gamma aluminum oxide (γ-Al_2O_3), and copper oxide (CuO), were added into distilled water (as base fluid) to prepare stable nanofluids (as injection fluids) for base oil recovery. The base oil obtained by Pouyan Sial Azar Company, Iran. Table (1) shows the physical properties of the utilized nanoparticles. Due to the limitations of oil recovery, to reduce interfacial tension between the aqueous phase and oil, sodium dodecyl sulfate (SDS, obtained by Merck, Germany) and xanthan gum (obtained by Merck, Germany) were employed as surfactants in preparing all nanofluids. This resulted in development of the stable suspension nanofluids. Note that, Considering that with the increase of SDS concentration up to the critical micelle concentration, the amount of interfacial tension decreases, and however with increasing the concentration after the critical micelle concentration, the interfacial tension does not change significantly, therefore SDS with a purity of 85 %wt and with a critical micelle concentration (CMC) of 7.3 mM [36] were prepared. Additionally, xanthan gum had concentration of 0.5 %wt. The reason to use xanthan gum was that, the incorporation of polymers in nanofluids

enhances the stability of nanoparticle distribution, and nanopolymer suspensions can enhance the capacity of nanoparticles to alter wettability and equilibrium states rapidly than polymer-free nanofluids [37-39].

Table 1: Physical characteristics of nanoparticles.

Material	Symbol	Manufacturer	Morphology	Specific surface area (m^2/g)	Color	Purity (%)	Particle size (nm)	Particle type
Titanium dioxide	TiO_2	US-Nano	Nanopowder, spherical	200	White	99.9	22	Anatase
Aluminum oxide	Al_2O_3	US-Nano	Nanopowder, spherical	138	White	99.6	20	Gamma
Copper oxide	CuO	US-Nano	Nanopowder, spherical	35	Black	99.9	42	_____

2.2. Solutions preparation and stability

All nanofluid samples were prepared in a two-step procedure as demonstrated schematically in Figure (1). Initially, an ultrasonic stirrer with a probe (Hielscher - UP400S, Germany) under ultrasonic waves (24 kHz and 400 W) was used to disperse 0.2 g of each nanoparticle and 7.3 mM SDS in 20 ml of distilled water for 25 minutes. Simultaneously, a magnetic stirrer (ALFA - HS860, Iran) was used to prepare a xanthan gum solution in another 20 ml of distilled water at a speed of 300 rpm. Figure (2) depicts the addition of surfactant to the solution, followed by 30 minutes of stirring to produce stable nanofluid samples. The zeta potential test was conducted (Nanotrac Wave-Microtrac, USA) to evaluate the stability as well as characterize the particle size and distribution. According to the DLVO theory, the van der Waals attraction forces enhance, and the unstable solution and particles stick together if the zeta potential falls below a specific threshold [40, 27]. Studies suggested that a nanofluid is stable if its zeta potential is greater than +30 mV or less than -30 mV [41]. Table (2) displays the measured zeta potential for the nanofluids 20 days after their preparation. The findings demonstrate the prepared nanofluid solutions' potential stability even after 20 days, indicating no sedimentation and colligation of the nanoparticles and emphasizing prepared nanofluids great ability for frequent application in long term.

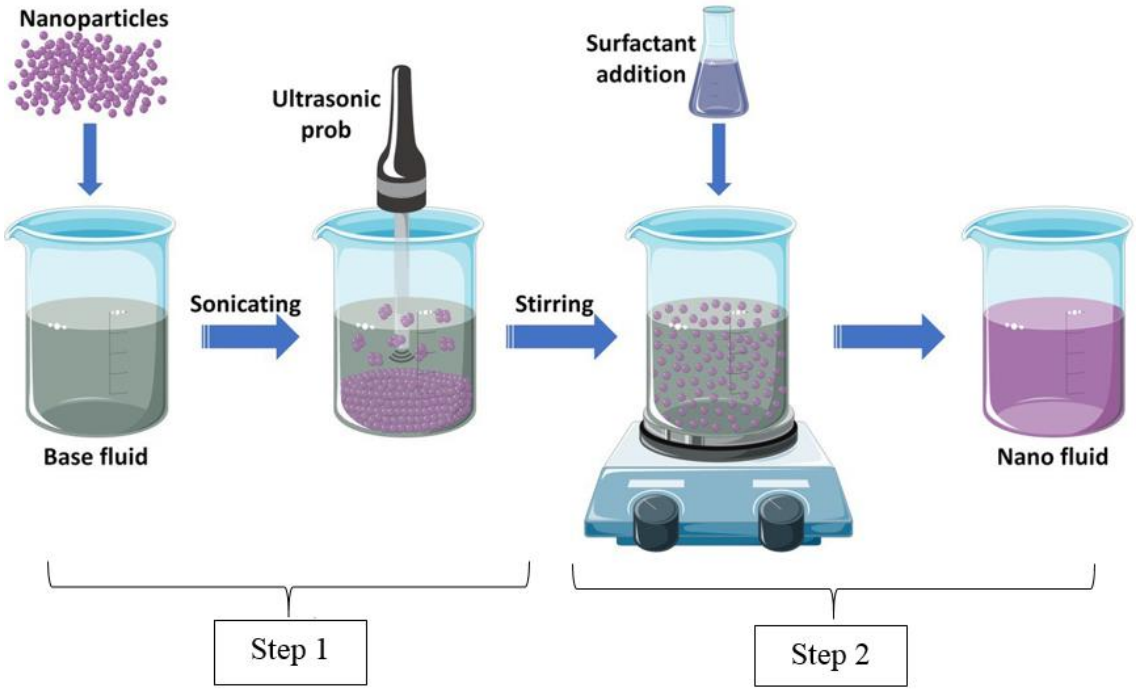

Figure 1: Schematic of the two-step process to prepare nanofluids.

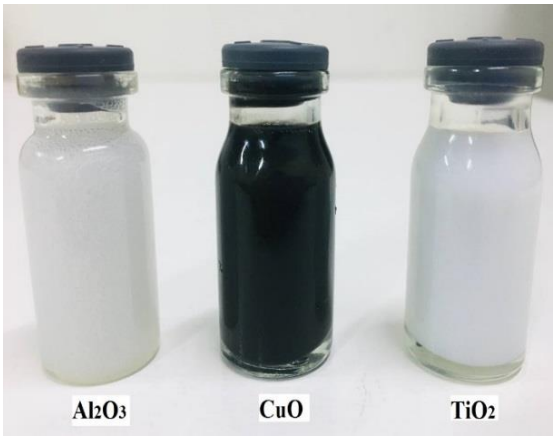

Figure 2: Prepared nanofluid samples.

Table 2: Zeta potential data of nanofluids 20 days after preparation.

Nanofluid	Zeta potential (mV)	Particle size
TiO_2	+42.4	29.1 nm:100%
Al_2O_3	+78.9	28.93 nm:100%
CuO	+52.9	33.1 nm:89.9%

2.3. Experimental Setup

The experimental setup consists of a double-walled reservoir. The reservoir itself is made of interconnected two cylindrical glass pipes with length of 51 cm. The outer cylinder (wall) serves as a thermal insulation, preventing heat dissipation to the external surroundings during the hot fluid injection. The inner cylinder measures 1 cm in diameter and 40 ml in bulk volume. The spherical glass beads with 2 mm diameter and a 35% porosity are employed as porous medium positioned within the double-walled reservoir. Totally, 14 ml of saturated base oil is contained within the porous medium. A syringe pump (Soraco-SP100, Iran) with flow control capability is employed to inject cold/hot fluids into the reservoir. The injected fluids are heated in a hot water bath. In addition, a stainless probe thermometer (Dallas-DS18B20, Iran) was used to indicate and adjust the temperature of the injected fluid just before entering the porous medium. A camera (Canon-7D EOS, Japan) was used to take photographs throughout each experiment in order to document the fluid flow patterns that occurs within the porous medium. Fluids are upward pumped from the bottom of the reservoir (anti-gravity) and exit from the top. The base oil is employed as displaced fluid, and water and nanofluids are injected as displacing fluids into the porous medium to recover oil. The base oil is injected into the reservoir 72 hours prior to each experiment to aid in more ageing. After each experiment, the glass beads were washed with methanol, toluene, and distilled water. Besides, all tests were performed at ambient pressure (1 atmosphere) and with an identical injection period (160 minutes).

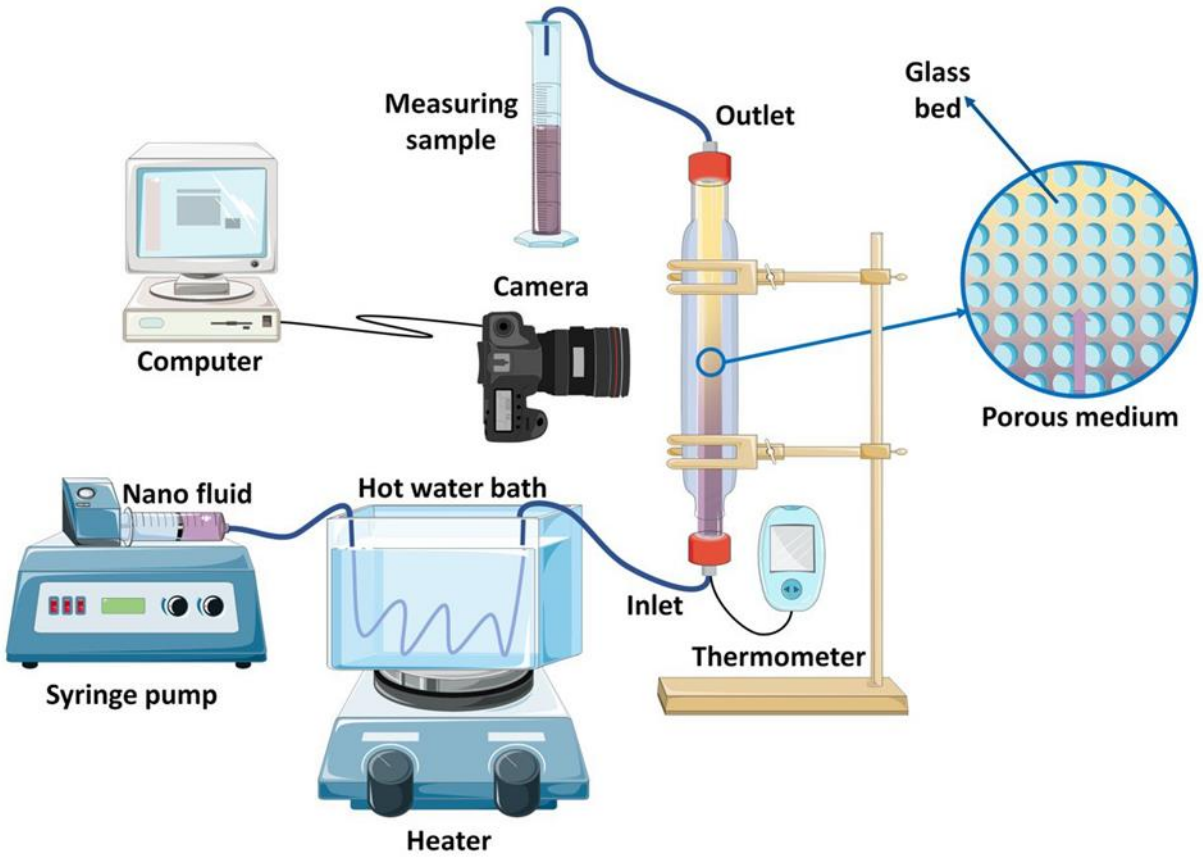

Figure 3: Schematic of the experimental setup including double-walled reservoir and its porous medium core, hot water bath, syringe pump, data recording system, and high-resolution camera.

2.4. Analysis

2.4.1. Characterization tests

Fourier transform infrared spectroscopic (FTIR, Tensor 27- Bruker, Germany) and X-ray diffraction (XRD, SIEMENS-D 5000, 40 Kv, 30 mA, Source: Cu, Germany) analyses were carried out to evaluate the composition and crystal arrangement of the synthesized nanoparticles. In addition, the morphological characteristics and stability of nanoparticles were determined using a field emission scanning electron microscope (FESEM, Tescan-MIRA 3, Czech Republic) analyses.

2.4.1.1. FTIR

As mentioned, FTIR tests were used to study the functional groups presence in nanoparticles. As shown in Figure 4a, the stretching vibration of Ti-O-Ti was indicated by the broad absorption peak in the range of 400-800 cm^{-1} attributed to titanium dioxide nanoparticles [42]. A further indication of the presence of Ti-O stretching vibration was related to the peaks in the range of 977-1049 cm^{-1} [42]. Moreover, the anatase phase of titanium dioxide nanoparticles was demonstrated by the presence of a broad absorption peak in the 400–1000 cm^{-1} range. Additionally, the hydroxyl group's bending and stretching vibrations associated with water absorption on nanoparticle surfaces were attributed to the 1632 and 3414 cm^{-1} peaks, respectively [43]. The existence of moisture in the specimens and potassium bromide employed to prepare tablets for measuring the FT-IR spectrum, can be deduced from the peaks that appeared at the wavelengths of 1135, 1400, and 2853 cm^{-1}, respectively [42]. The vibration of the Cu-O stretching bonds was indicated by the peaks at wavelengths of 534 and 584 cm^{-1} in the copper oxide nanoparticles' infrared spectrum as shown in Figure 4b [44]. The bending and stretching vibration of water molecules absorbed on the surface of the nanomaterial account for the peaks around 1632 and 3500 cm^{-1} [45]. There were additional peaks as a result of the prepared tablet's moisture content [46]. Al-O-Al bonds, AlO_4 sites, and AlO_6 sites were all attributable to vibrational peaks at wavelengths of 500-900 cm^{-1} in the aluminum oxide nanoparticles' infrared pattern shown in Figure 4c [47, 48]. The bending and stretching vibrations of hydroxyl groups associated with the water absorbed on the sample's surface generated the peaks at wavelengths 2925 and 3452 cm^{-1} [49]. Other peaks in the spectrum were made by moisture in potassium bromide employed to produce tablets [47].

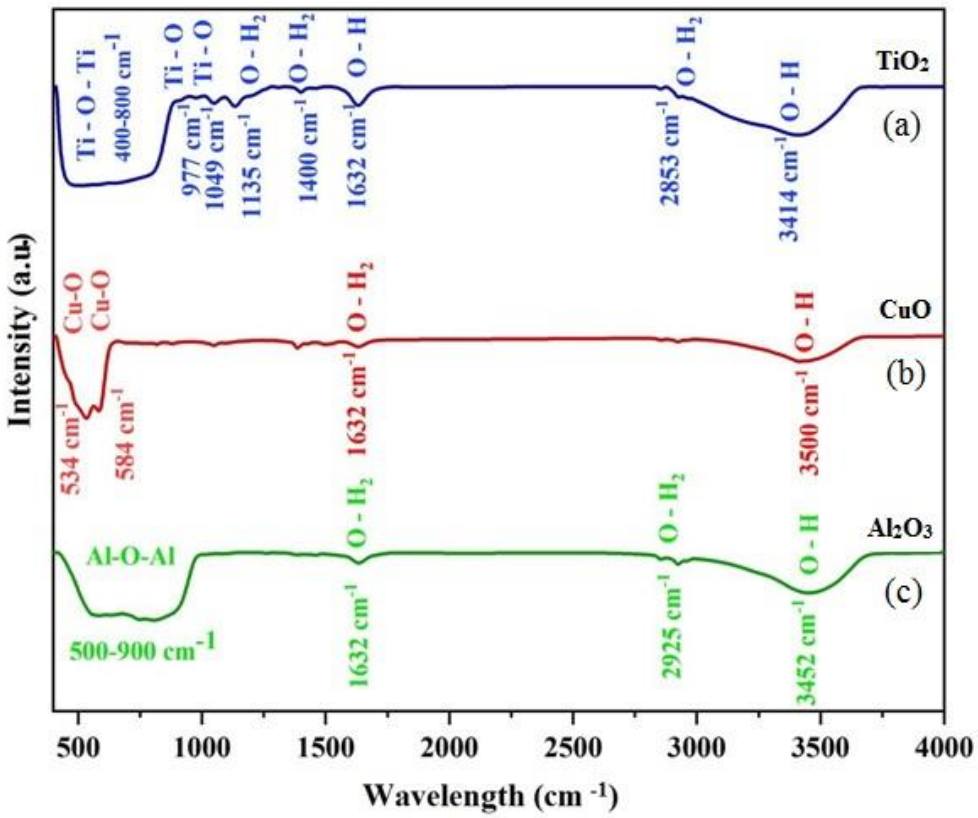

Figure 4: Infrared spectrum taken from the nanoparticle samples.

2.4.1.2. XRD

The crystal structure of titanium dioxide, copper oxide, and aluminum oxide nanoparticles was investigated using X-ray diffraction spectrum shown in Figure 5. Diffraction peaks at 2θs of 25.3, 36.9, 37.7, 38.5, 48.0, 53.8, 55.0, 62.0, 62.6, 68.7, 70.2, 75.05, and 76.0 discovered in titanium dioxide nanoparticles can be classified in reflective surfaces (011), (013), (004), (112), (020), (015), (121), (123), (024), (116), (220), (125), and (031), respectively. The anatase phase of titanium dioxide nanoparticles, in which the atomic arrangement is tetrahedral, is indicated by these peaks and their associated reflection levels related to the reference number of 96-720-6076 and the standard peaks provided in different references [50, 51]. The high purity of the material can be identified by the diffraction pattern of titanium dioxide nanoparticles and the existence of sharp peaks without the presence of secondary peaks. The width of the domain at the height of the half peaks with higher intensity in the X-ray diffraction pattern was used to measure the mean size of titanium dioxide nanoparticle crystals based on the equation (1) (Debye-Scherrer equation) [52].

$$D = K\lambda/\beta \cos\theta \quad (1)$$

Where D represents the size of nanoparticle crystals in nanometers. K, the equation's constant, has a value of 0.9 for homogeneous specimens, and λ pertains to the wavelength of the beam radiated by the lamp employed by the XRD device. The lamp is made of copper, and its λ is 0.15406 nm. β represents the domain width at half height, which corresponds to peaks with higher intensities in the sample spectrum, and θ represents the diffraction angle in radians. The mean crystal size of titanium dioxide nanoparticles was 22.4 nm, according to this equation. Equation (2) and equation (3) (Bragg equation) were used to determine the titanium dioxide nanoparticles' tetragonal crystal lattice's parameters [51]:

$$\frac{1}{d^2} = \frac{h^2}{a^2} + \frac{k^2}{b^2} + \frac{l^2}{c^2} \quad (2)$$

$$d = n\lambda/\sin\theta \quad (3)$$

The Miller indices or reflective surfaces are represented by h, k, and l in equation (2). The lattice constants are also denoted by a, b, and c, while d represents the distance between atomic planes. In addition, in equation (3), n represents the order of diffraction, and the number 1 is assigned to the first order. λ represents the X-ray wavelength emitted by the copper lamp. The diffraction angle is expressed as θ in radians. a=b=7.17 and c=9.54 Å are the lattice constants for tetrahedral crystals of titanium dioxide, and all angles between them are 90°, according to these equations. Each crystalline unit has a volume of 491.43 cubic Å. Reflective surfaces of (110), (001), (11 -1), (111), (20 -2), (020), (202), (11 -3), (31 -1), (220), (311), (220), and (22 -2) were associated with the diffraction peaks at 2θs of 32.4, 35.4, 35.5, 38.7, 48.7, 53.4, 58.3, 61.5, 66.2, 68.1, 72.4, and 75.2, respectively in X-ray diffraction spectrum of copper oxide nanoparticles. The crystal unit cell structure is monoclinic, according to the acquired diffraction pattern consistent with reference number of 96-901-4581 and literature [53-55]. Additionally, the high purity of the nanomaterial is responsible for the lack of secondary peaks. The mean particle size and lattice constants were calculated using Equations (1), (2), and (3). Copper oxide nanoparticles had a mean size of 42.7 nm. The a=21.58, b=3.42, and c=5.07 were lattice constants of copper oxide nanoparticles, and the angle between them was equal to α=γ=90° and β=54.99°, respectively, and each lattice unit cell of the crystal network had a volume of 375.02 cubic Å. There is correspondence between the peaks of 22.5, 32.0, 37.3, 39.6, 45.4, 46.2, 53.0, 60.1, 67.1, and 76.5 with reflective surfaces (111), (202), (311), (222), (400), (313), (422), (333), (513), and (533),

respectively, in the X-ray diffraction pattern of aluminum oxide nanoparticles. The shape of the aluminum oxide nanoparticles' crystal lattice was cubic, according to the acquired diffraction pattern, and corresponded to the reference number 96-120-0016 and literature [56, 57]. The mean size of nanoparticles was determined to be 20.5 nm, and the a=b=c=7.98 Å were lattice constants with a 90° angle between them. Each unit cell of the aluminum oxide crystalline lattice has a volume of 508.99 cubic Å.

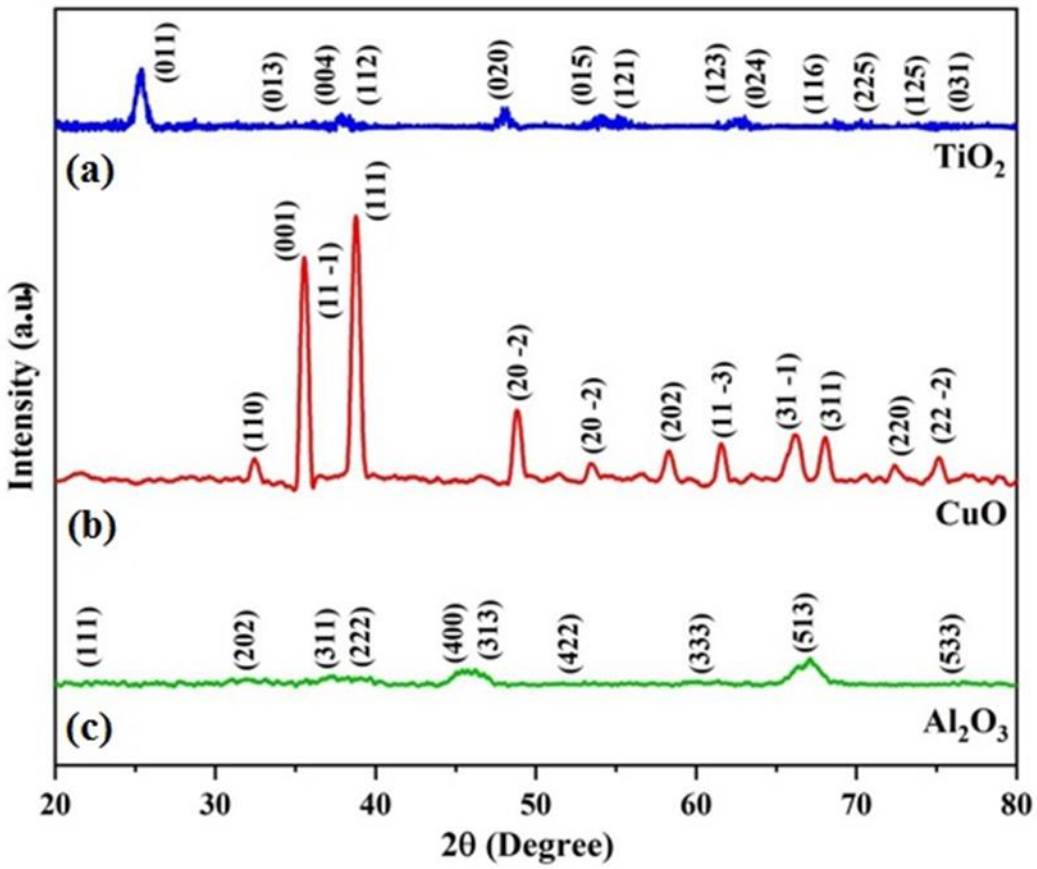

Figure 5: X-ray diffraction pattern of nanoparticles used.

2.4.1.3. FESEM

The morphology and structure of nanomaterials were studied using field emission scanning electron microscope (FESEM) test. Various scales of 200 nm, 500 nm, and 1 μm were used to capture FESEM images. Figure 6a-c demonstrates that the nanoparticles of titanium dioxide are randomly dispersed and have no particular orientation; they are nearly spherical and have a smooth and soft exterior. These nanostructures have dimensions ranging from 22 to 89 nm. The acquired findings agree with previous investigations and XRD results [58, 59]. Copper oxide nanostructures can be observed in Figure 6d-f. The recorded images show that the copper oxide nanostructures are nearly spherical and have disordered and clump arrangements. According to previous studies and the findings from the XRD pattern, copper oxide particles size is between 42 and 200 in good agreement with literature [60]. Aluminum oxide nanoparticles are depicted in Figure 6g-i. Amorphous nanostructures are arranged in an irregular and dense pattern, according to morphological investigations [61]. These nanoparticles have dimensions ranging from 20 to 60 nm [48]. Overall, the information acquired from FESEM images is compatible with the earlier investigation and XRD data [62].

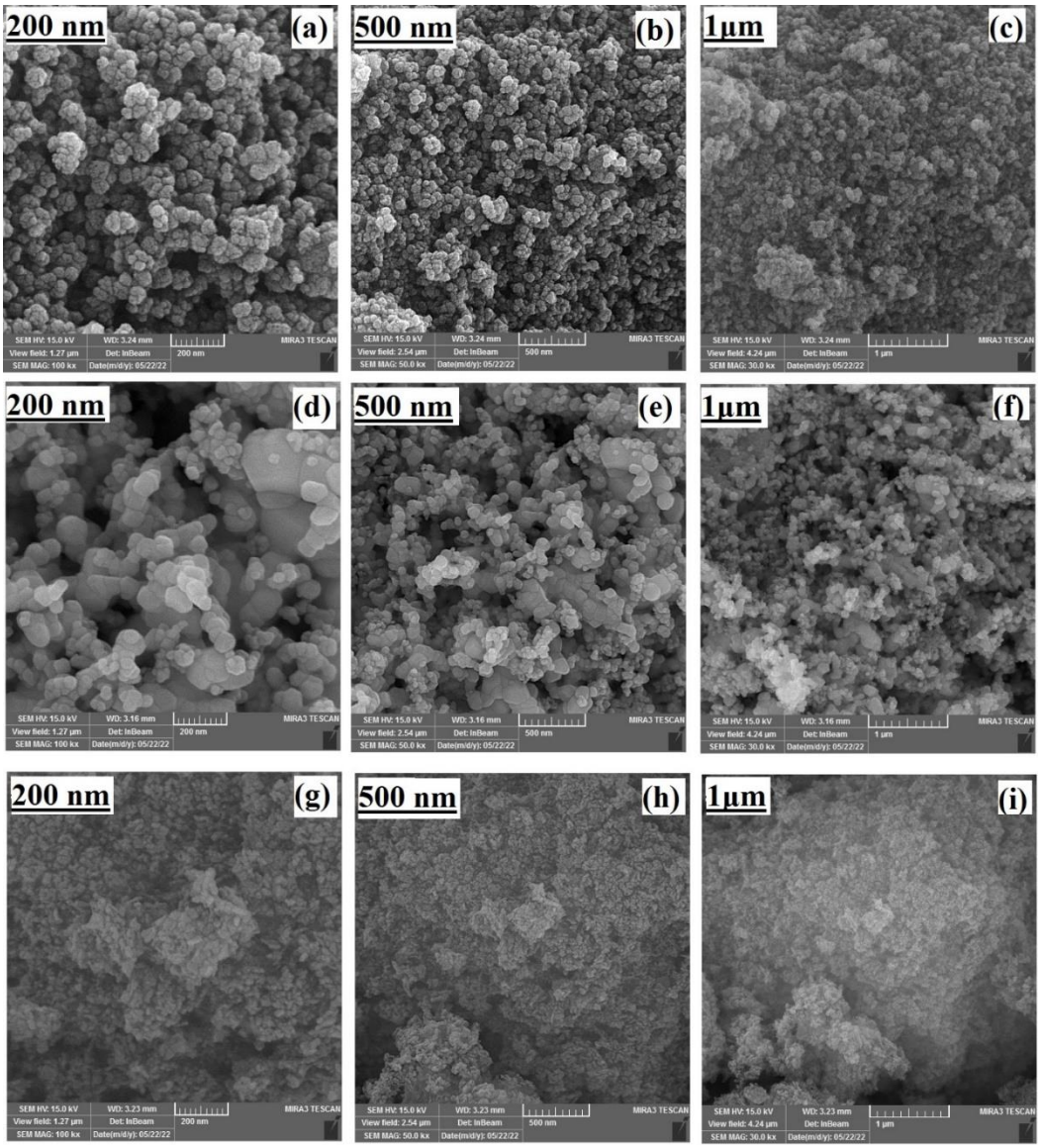

Figure 6: FESEM images of (a-c) TiO_2, (d-f) CuO, and (g-i) Al_2O_3 nanoparticles.

2.4.2. Viscosity measurement

The base oil and displacing fluids viscosities were measured using a viscometer (BROOKFIELD, DV-II+Pro, USA). The results have been shown in Table 3.

Table 3: Physical properties of the utilized fluids.

Fluid	density (g/cc)	Kinematic viscosity at 25°C (cSt)	Dynamic viscosity at 25°C (cP)	Kinematic viscosity at 90°C (cSt)	Dynamic viscosity at 90°C (cP)
Base Oil	0.895	150.77	134.93	70.52	63.11
Distilled Water	0.998	0.896	0.894	0.316	0.315
TiO_2 Nanofluid	1.05	69.15	72.6	32.37	33.98
Al_2O_3 Nanofluid	1.15	56.75	65.26	25.22	29
CuO Nanofluid	1.1	89.86	98.84	37.83	41.61

2.4.3. Interfacial tension measurement

Interfacial tension between base oil and injected fluids at various temperatures was measured using a tensiometer (Kruss-K20EASYDYN, Germany). The results have been presented in Table 4. The findings revealed that the interfacial tension between base oil and nanofluids is significantly decreased by increasing the temperature and adding nanoparticle to water. Compared to the water-oil interfacial tension, its magnitude is reduced by 94.76, 92, and 90.5% for Al_2O_3, CuO, and TiO_2 nanofluids, respectively. In nanofluids, the ability to absorb stable surfactants and transfer them to the oil-water interface is improved by adding nanoparticles [27], SDS surfactants [63], and xanthan gum polymer. Consequently, this results in an enhancement of the surfactant monomers' number and so a significant reduction in the interfacial tension. Interfacial tension reduction weakens the oil-fluid tension and interactions at the interface, making displacement of trapped oil droplets from pores relatively easy, resulting in enhanced oil recovery.

Table 4: Measured interfacial tension between base oil and injected fluids.

Fluids	Interfacial tension at 25°C (mN/m)	Interfacial tension at 90°C (mN/m)
Oil-Water	45.03	37.92
Oil-TiO_2	4.3	3.57
Oil-Al_2O_3	2.36	1.86
Oil-CuO	3.7	3.02

2.4.4. Contact angle measurement

To better analyze the results the contact angle between the fluids and the reservoir glass was measured using a suitable device (Jikan CAG-20, Iran) utilizing the

hanging drop technique. The results have been shown in Figure 7. As shown, adding the nanoparticles and surfactant substantially lowers the contact angle due to chemical and physical interactions, such as the hydroxyl group interaction with nanoparticles adsorbed on the solid surface, in addition to the existence of forces such as electrostatics, van der Waals, and also structural surface forces. In other words, nanoparticles increase the hydrophilicity of the glass surface. It is worth mentioning that increasing the concentration of nanoparticles in the preparation of solutions has led to an increase in the absorption percentage of injected nanofluids on the solid surface. Also, due to the fact that gamma alumina nanoparticles used in the preparation of Al_2O_3 nanofluid are naturally hydrophilic, solutions of this nanofluid have shown more potential for wettability alteration. Injection of nanofluids enhances the relative permeability of oil by decreasing the contact angle and altering wettability to hydrophilicity. Thus, this is one of the appropriate mechanisms in enhancing oil recovery. In this scenario, the oil strives to migrate from areas close to the walls towards the center, making the operation easier and more efficient.

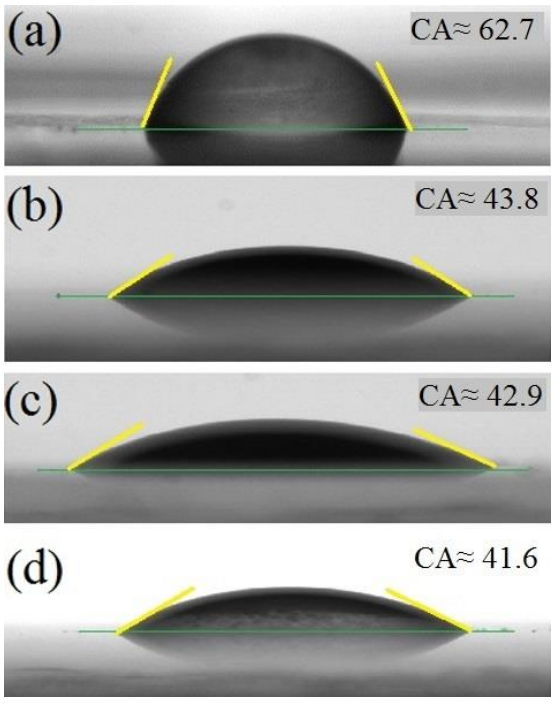

Figure 7: Contact angle between reservoir glass surface and (a) Water drop, (b) CuO nanofluid drop, (c) TiO_2 nanofluid drop, and (d) Al_2O_3 nanofluid drop.

3. Results and discussion

3.1. Water injection

To study effects of flowrate on oil recovery, distilled water was injected at different flowrates of 0.1, 0.2, 0.3, and 0.4 mL/min into the double-walled reservoir in both anti-gravity and gravity-aligned directions at temperature of 25 °C. Variation of the volume of the recovered oil during the water injection at various flowrates has shown in Figures (8) and (9). It is evident that the volume of the recovered oil increased when the flowrate decreased from 0.4 to 0.1 mL/min, regardless of the injection direction. According to the results, the optimal flowrate for displacing fluid injection was 0.1 mL/min. This is attributed to the decrease in injection velocity and the increased in injected fluid resident time which results in the displacement through small pores, and the slow migration through the pores, ending in the fingers reduction and the displacement stabilization. For similar reason, more oil volume was recovered by reducing the flowrate when injecting upwards (anti-gravity) compared to the downward injection (gravity-aligned).

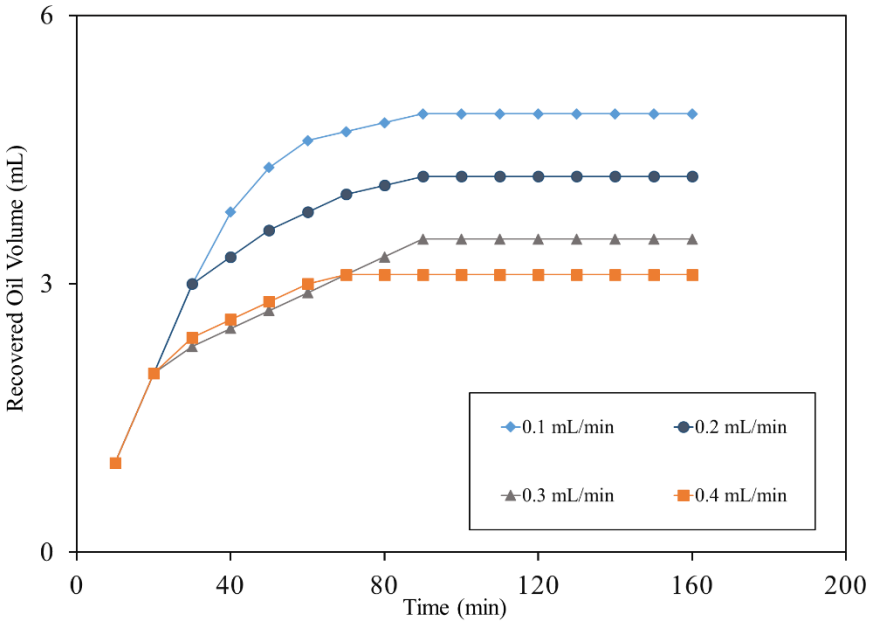

Figure 8: Recovered oil volume during water injection in gravity-aligned direction for different flowrates at 25 °C.

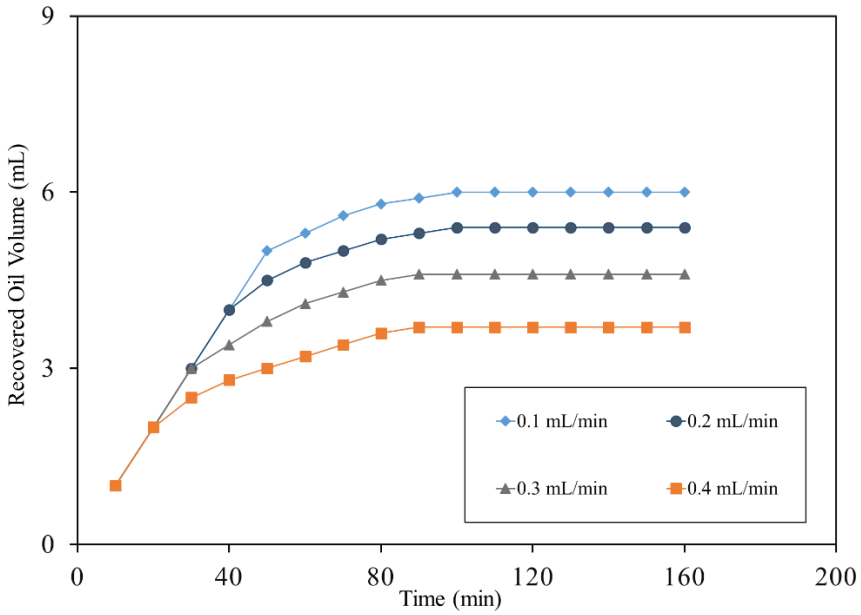

Figure 9: Recovered oil volume during water injection in anti-gravity direction for different flowrates at 25 °C.

Results indicates that the volume of recovered oil enhanced by 18.3% in anti-gravity injection at a flowrate of 0.1 mL/min compared to injection gravity-aligned direction for the same flowrate. Given the fact that water fluid has a higher density than oil, on the one hand, and according to the equation (4) which uses gravitational force to accelerate the downward injection of water fluid, this results in the early combining of water and oil phases. Following that, the flux and flowrate increases in accordance with equations (5) and (6). Consequently, the injected fluid finds paths through the larger pores only, and oil recovery reduces.

$$\Delta p = \rho g h \tag{4}$$

Where Δp denotes the hydrostatic pressure difference in Pa, ρ represents the density in Kg/m^3, g denotes the gravitational acceleration in m/s^2, and h denotes the height in m.

$$u = k\Delta p/\mu L \tag{5}$$

Where u represents the artificial velocity in m/s, k represents a porous medium permeability in m^2, Δp denotes the pressure drop (hydrostatic pressure difference) in Pa, μ indicates the dynamic viscosity of fluid in Pa.s, and L is a distance in m.

The velocity at which the fluid is moving through the pores, is not represented by the value of u in equation (5), the flow velocity or more precisely, the intrinsic velocity is represented by equation (6).

$$V = \frac{u}{\phi} \tag{6}$$

Where V represents the intrinsic velocity in m/s, and ϕ indicates the porosity percentage.

In anti-gravity direction fluid injection, there is no weight force, and the external force (induced by injected/displacing fluid) is the only effective factor in this condition. Hence, compared to the downward injection, the velocity of displacing fluid is slower during the anti-gravity injection. The fluid-fluid interfacial morphology is stable and wider. It is worth noting that a drop of black ink was added to the water to more effectively investigate the water fluid flow pattern in the porous medium, despite the fact that there has been no difference in fluid's physical properties.

Figure (10) shows the injected flow pattern when blackened pure water was injected in gravity-aligned and antigravity directions with a constant flowrate of 0.1 mL/min at 25 °C. As shown in Figure 10-1, 10-2, and 10-3 when blackened water is injected in gravity-aligned direction its pathway does not cover the most part of the porous medium. The pathway is narrow and looks like a finger and channelized. In this injection type, the breakthrough time is 37 minutes. However, when the same fluid is injected in antigravity direction most part of the porous medium cross section is covered by blackened water. This kind of flow pattern enhances the breakthrough time/residence time of the blackened water from 37 to 52 minutes and eventually increases the oil recovery from 3.8 ml to 5.3 ml.

Figure 10: The blackened water distribution pattern in gravity-aligned direction; (1) at t=30min, (2) when breakthrough happens at t=32min, and (3) at t=90min. The blackened water distribution pattern in antigravity direction; (4) at t=50min, (5) when break through happens at t=57min, and (6) at t=95min.

3.2. Nanofluid injection

To explore the effects of nanoparticle in oil recovery, injection of TiO_2, γ-Al_2O_3, and CuO nanofluids was carried out. For this purpose, concentration of 0.25, 0.5, and 1%wt from each nanoparticle in base fluid was investigated. Diagrams of the recovered oil volume versus the antigravity injection time of nanofluids with flowrate 0.1 mL/min at 25 °C have been shown in Figure 11. The findings demonstrated that as nanoparticle concentration increases, the volume of the recovered oil also increases as well. This is due to the increase in density of the nanofluid with increasing the nanoparticle concentration. As shown in the Figure 11, the optimal concentration of investigated nanoparticles maybe considered 1%wt. Moreover, for two reasons, the volume of the recovered oil by injecting γ-Al_2O_3 nanofluid at each concentration is greater than that of similar concentrations of CuO and TiO_2 nanofluids (see Table 5). The first reason is the Al_2O_3 nanofluid has higher density than the other nanofluids. The heavier the injected fluid, the improved and gentler the fluid displacement in the porous medium during the antigravity injection. The second reason is due to the wettability of γ-Al_2O_3 nanofluid. This nanofluid is more hydrophilic than the other two nanofluids. As a consequence, more oil from porous medium is recovered.

Note that, in order to ensure the reliability of the results, all the experiments were repeated 3 times and due to the error rate of less than 1%, the results of all the tests were reported as their average. Furthermore, the error rate less than 1% caused by repeating the experiments in each of the cases indicates the reliability of the obtained results.

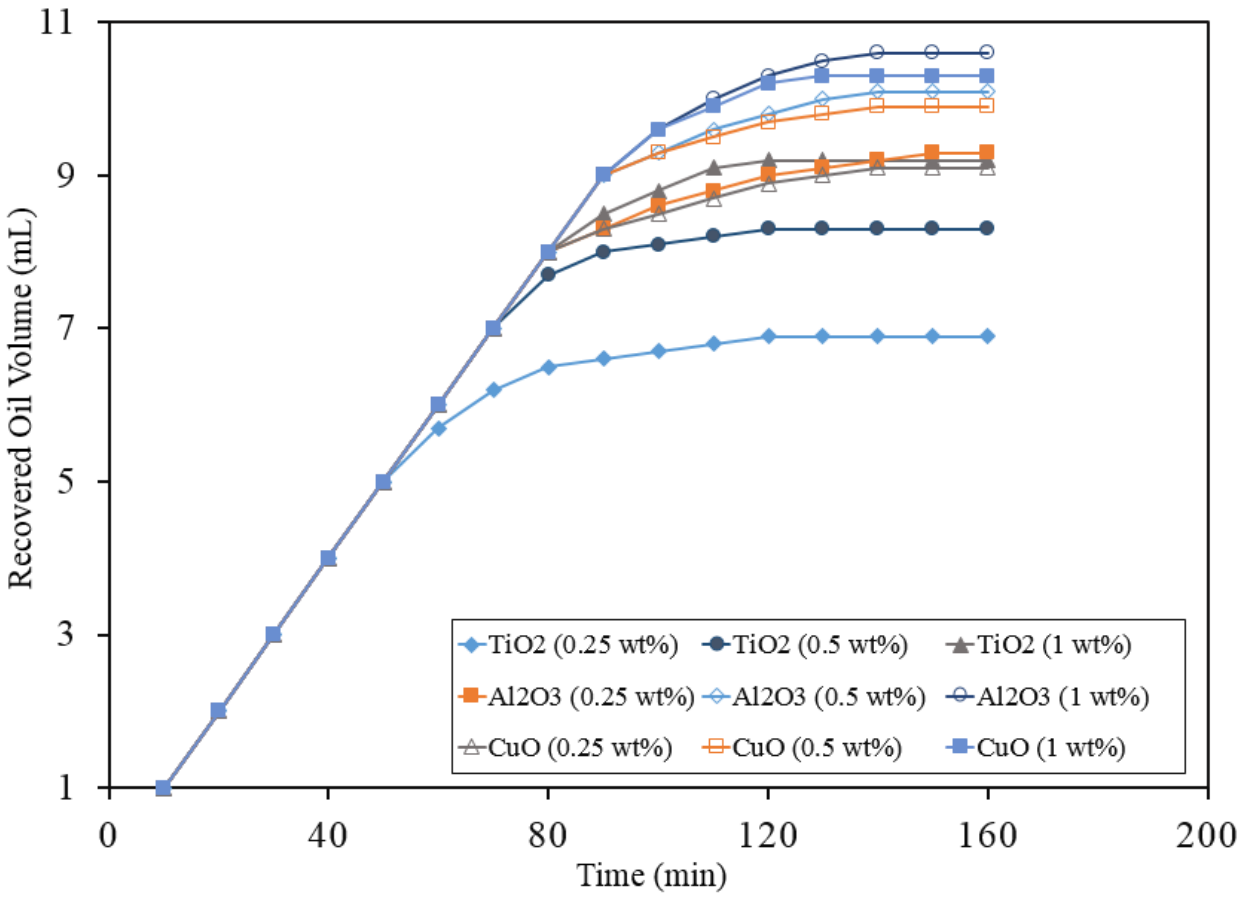

Figure 11: Recovered oil volume during the time when nanofluids were injected with different concentrations with flowrate of 0.1 mL/min at 25 °C in the antigravity injection.

Table 5: Volume of recovered oil when injecting nanofluid at different concentrations.

Type of Nanofluid	Concentration(%wt)	Recovered Oil Volume(mL)	Error rate caused by 3 repetitions of experiments (%)
TiO_2	0.25	6.9	≈0.5
	0.5	8.3	<1
	1	9.2	<0.5
CuO	0.25	9.1	≈0.5
	0.5	9.9	<1
	1	10.3	<1
γ-Al_2O_3	0.25	9.3	<1
	0.5	10.1	<1
	1	10.6	<0.5

As known, the most effective parameters on the enhanced oil recovery can be determined using the dimensionless parameters e.g., capillary number, which is

described as the proportion of viscous forces to the interfacial forces of two immiscible fluids according to the equation (7) [64].

$$Ca = \frac{\mu V}{\sigma} \quad (7)$$

Where μ represents the dynamic viscosity of the injected fluid, V maybe considered as average velocity of the injected fluid, and σ represents the interfacial tension of two fluids.

Since the velocity of the injected nanofluids is only affected by an external force (injection flowrate) in antigravity injection, the amount of interfacial tension and dynamic viscosity is responsible for the volume of the recovered oil when using different nanofluids according to the equation (7). Compared to the other nanofluids, although the γ-Al_2O_3 nanofluid has lower dynamic viscosity, however interfacial tension between oil and γ-Al_2O_3 is lower than those of the others (see Tables 3, 4). The interfacial tension dominants over the viscosity factor, and the capillary number of the injected γ-Al_2O_3 nanofluid decreases. As a result, the residence time of the γ-Al_2O_3 increases resulting in oil saturation reduction in porous medium and so oil recovery enhancement. Therefore, this is to confirm that interfacial tension is the most effective factor in enhancing oil recovery.

Figures 12, 13, and 14 show the flow patterns of the injected fluids including TiO_2, CuO, and γ-Al_2O_3 nanofluids for gravity-aligned and antigravity injections when injected flowrate is 0.1 mL/min and temperature is 25 °C. Note that in all figures oil has yellowish color. According to the flow patterns, even though the interfacial tension reduction increases the possibility of the miscibility of the injected fluid with oil, it maybe concluded that during the antigravity injection of nanofluids, the injected fluid covers most parts of the porous medium cross-sectional area along with the reduction in channeling and fingering pattern compared to the gravity-aligned injections. Overall, in antigravity injection, the amount of the recovered oil from porous medium because of growth of the breakthrough time has increased substantially.

However, it is important to note that, regardless of the injection direction the recovered oil volume when nanofluids are injected is higher than that of water fluid injection despite the fact that the interfacial tension between nanofluids and water is lower than that of oil-water.

For all injected fluids the maximum oil recovery in gravity-aligned and antigravity injections when injected flowrate is 0.1 mL/min and temperature is 25 °C have been

shown in Figure (15). It is clear that nanofluids have the potential to substantially enhance the oil recovery rate compared to the pure water. As shown, γ-Al_2O_3, CuO, and TiO_2 nanofluids injection improve oil recovery efficiency by 43.5%, 41.8%, and 34.9%, respectively compared to the pure water results.

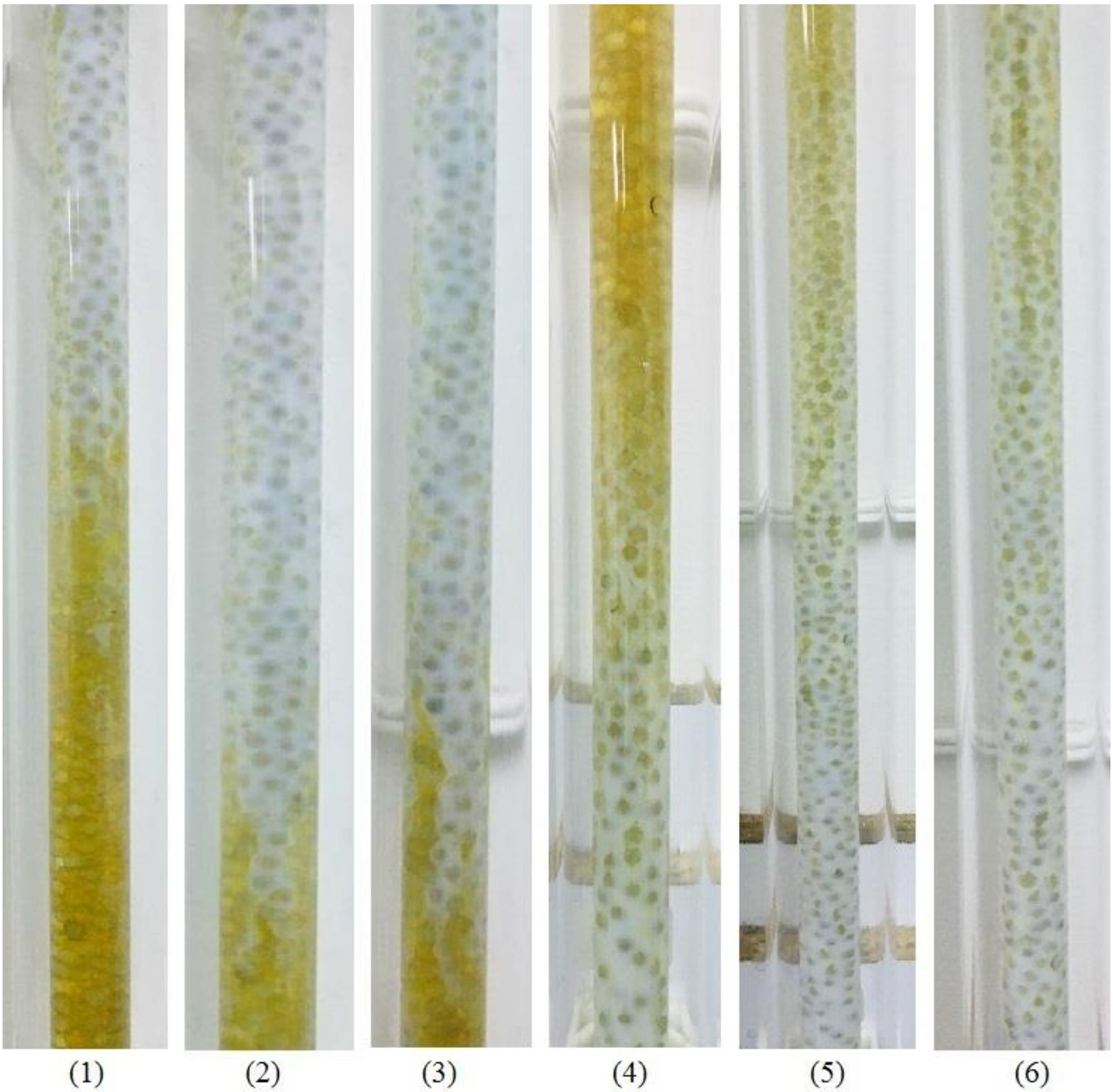

Figure 12: The TiO_2 nanofluid distribution pattern in gravity-aligned direction injection; (1) at t=60min, (2) when breakthrough happens at t=65min, and (3) at t=100min. The TiO_2 nanofluid distribution pattern in

antigravity direction injection; (4) at t=80min, (5) when breakthrough happens at t=85min, and (6) at t=120min.

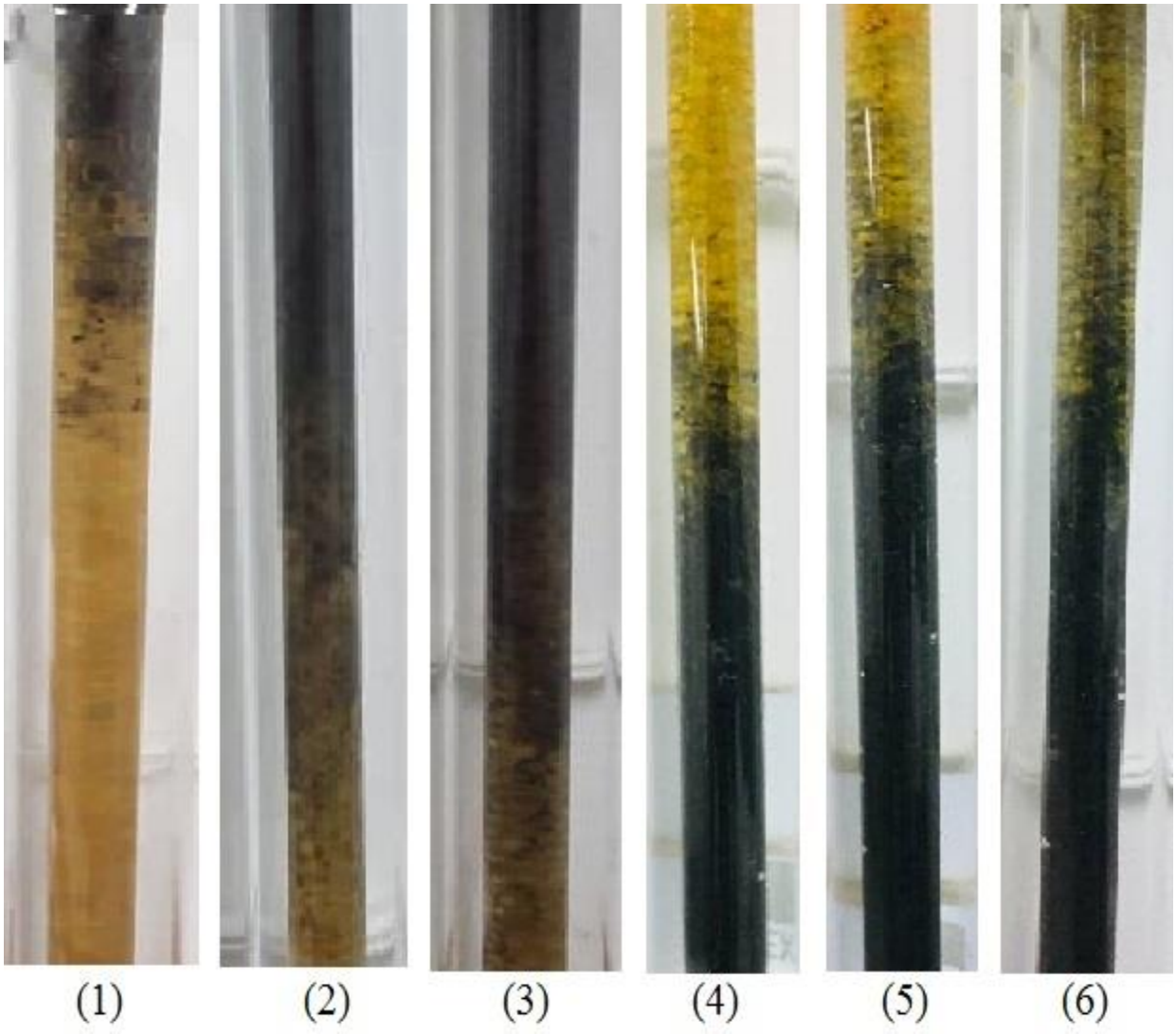

Figure 13: The CuO nanofluid distribution pattern in gravity-aligned direction injection (1) at t=70min, (2) when breakthrough happens at t=75min, and (3) at t=120min. The CuO nanofluid distribution pattern in antigravity direction injection; (4) at t=90min, (5) when breakthrough happens at t=94min, and (6) at t=130min.

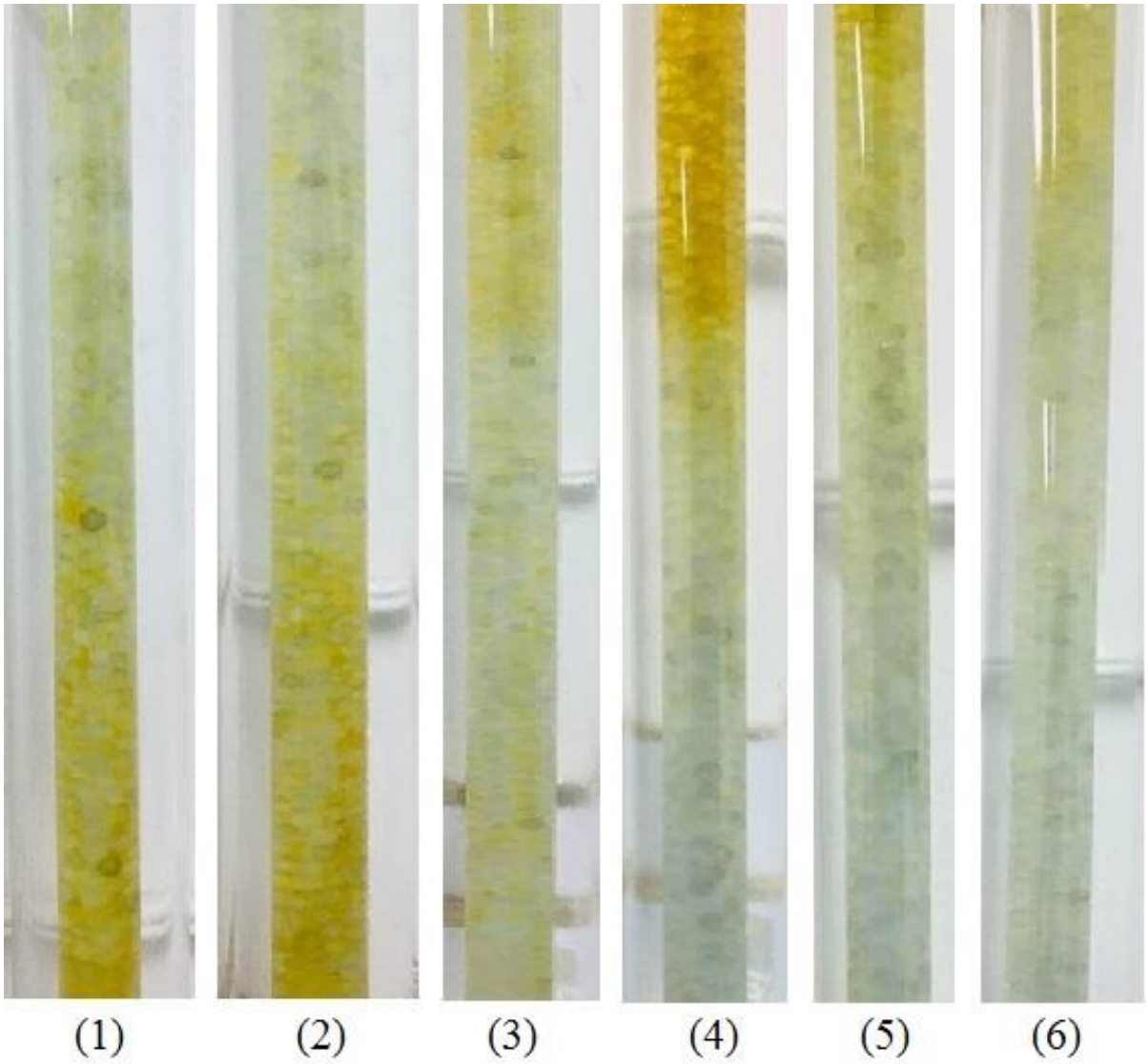

Figure 14: The γ-Al_2O_3 nanofluid distribution pattern in gravity-aligned injection direction; (1) at t=60min, (2) when breakthrough happens at t=63min, and (3) at t=130min. The γ-Al_2O_3 nanofluid distribution pattern in antigravity injection direction; (4) at t=90min, (5) when breakthrough happens at t=96min, and (6) at t=140min.

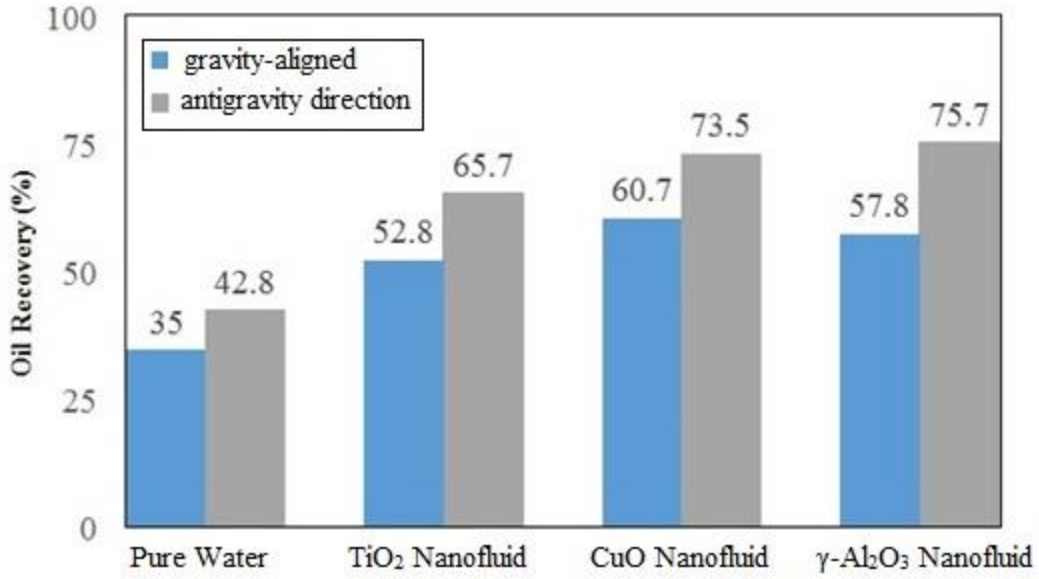

Figure 15: The maximum oil recovery by injecting pure water and nanofluids in gravity-aligned or antigravity direction with injection flowrate of 0.1 mL/min at 25 °C.

In gravity-aligned injection the Rayleigh–Taylor (RT) instability which is an instability of interface between two fluids of different densities employed to demonstrate how lighter fluid is pushing the heavier fluid in a porous medium is important to rationalize the fluid-fluid interfacial morphology [65]. This instability is described as proportion of the buoyancy forces to the penetration forces. By displacing the heavier fluid downwards with an equal volume of lighter fluid upward at interface, the potential energy will be lower than the initial state. Therefore, the growth of the perturbation leads to the release of more potential energy due to the displacement of denser material downwards and the movement of lighter materials upwards. In this scenario, Atwood's number given by equation (8) is employed to investigate the hydrodynamic (Rayleigh–Taylor) instabilities.

$$A = \frac{\rho_1 - \rho_2}{\rho_1 + \rho_2} \tag{8}$$

Where A represents Atwood number, ρ_1 indicates density of heavier fluid, and ρ_2 represents density of lighter fluid. For A close to 0, RT instability is low and for A close to 1, RT instability is high. In current study, in gravity-aligned direction as water/nanofluid is heavier than the oil so Atwood number looks to be an important parameter in determines the structure of the flow pattern. According to the calculated Atwood number for different fluids injection in gravity-aligned direction presented

in Table (6), someone may conclude that the large number of fingers and channeling are the reasons for less oil recovery during the injection in gravity-aligned direction. In contrast, during the antigravity injection due to the fact that, heavier fluid is injected from bottom of the porous medium the RT instability would not be important.

Table 6: Calculated Atwood number for gravity-aligned case.

Fluid-Fluid	Atwood number
Oil - Pure water	0.054
Oil - TiO_2 nanofluid	0.079
Oil - Al_2O_3 nanofluid	0.124
Oil - CuO nanofluid	0.102

3.3. Effect of injection temperature

To explore effects of the injection fluid temperature on the oil recovery, all fluids were injected at 25 °C and 90 °C. The modified capillarity number, Ca′, maybe written using equation (9). Where Ca′is defined by proportion of the viscous forces to the interfacial forces multiplied by the mobility ratio and the ratio of interfacial tension due to changes in the temperature of the fluids.

$$Ca' = \frac{\mu_1 V}{\sigma} \frac{\mu_2}{\mu_1} \frac{\sigma}{\sigma'} \quad (9)$$

Where μ_1 is the displacing fluid viscosity, and μ_2 is the displaced (oil) fluid viscosity. μ_2/μ_1 considers the additional impact of viscosity or mobility ratio due to the change in temperature on the capillary number [66]. Moreover, σ and σ′ represent interfacial tension before and after temperature change, respectively.

In liquids, viscous forces are caused by molecules that exert attractive forces on each other across the flow layers. In fact, it is these attractive forces that are responsible for the viscosity since it is difficult for individual molecules to move because they are tightly bound to their neighbors. Hence, the increase in temperature results in viscosity reduction due to the increase in the thermal energy of the particles and the easy overcoming on the attractive forces that connect them together. Also, an increase in temperature decreases the cohesive forces simultaneously because of increase in the rate of molecular interchange.

According to the viscosity results presented in Table (3), and considering that the increase in temperature makes the viscosity of injected fluid and oil to decrease almost to the same extent, therefore the viscosity ratio does not change very much with increasing the temperature. This is can be understandable using Hole theory [67]. According to this theory, there are vacancies or holes in a liquid. The liquid molecules keep on moving continuously into these vacancies. The vacancies also keep on moving around as otherwise the liquid will not be able to flow. This process however requires energy. Therefore, a liquid molecule needs some activation energy to move into a hole. As the activation energy becomes available when temperature increases, a liquid can flow more easily at higher temperature. Thus, viscosity decreases significantly with a rise in temperature.

On the other hand, the interfacial tension results presented in Table (4) indicate that the interfacial tension of the injected fluid and the oil decrease dramatically with the rise in temperature. The decrease in interfacial tension with increase of temperature is due to the fact that with increase in temperature, the kinetic energy of the molecules increases, and hence intermolecular attraction decreases. Thus, the interfacial tension decreases. This reduction for oil-water interfacial tension is 15.8% and for oil-Al_2O_3 nanofluid is 21.2%. As an important note, it must be said that, increasing the temperature will decrease the stability of the nanofluid solutions because of weakening the continuity of the three-dimensional networks of particles due to the increase in the distance between the nanoparticles and surfactant [27].

Thus, according to the equation (9) the modified capillary number increases as a result of interfacial tension reduction and negligible change in the viscosities ratio. Consequently, change in temperature emphasizes the importance of the interfacial tension change as the key important factor in enhancing oil recovery.

Figure (16) depicts the recovered oil volume during the time when water/nanofluid is injected at 25 °C or 90 °C with flowrate of 0.1 mL/min in antigravity direction. As shown, injection of γ-Al_2O_3 recovers more oil from the porous medium compared to the other injected fluids at the same temperature. Also, the results obtained along with the rate of error caused by the repetition of each of the experiments are reported in Table (7).

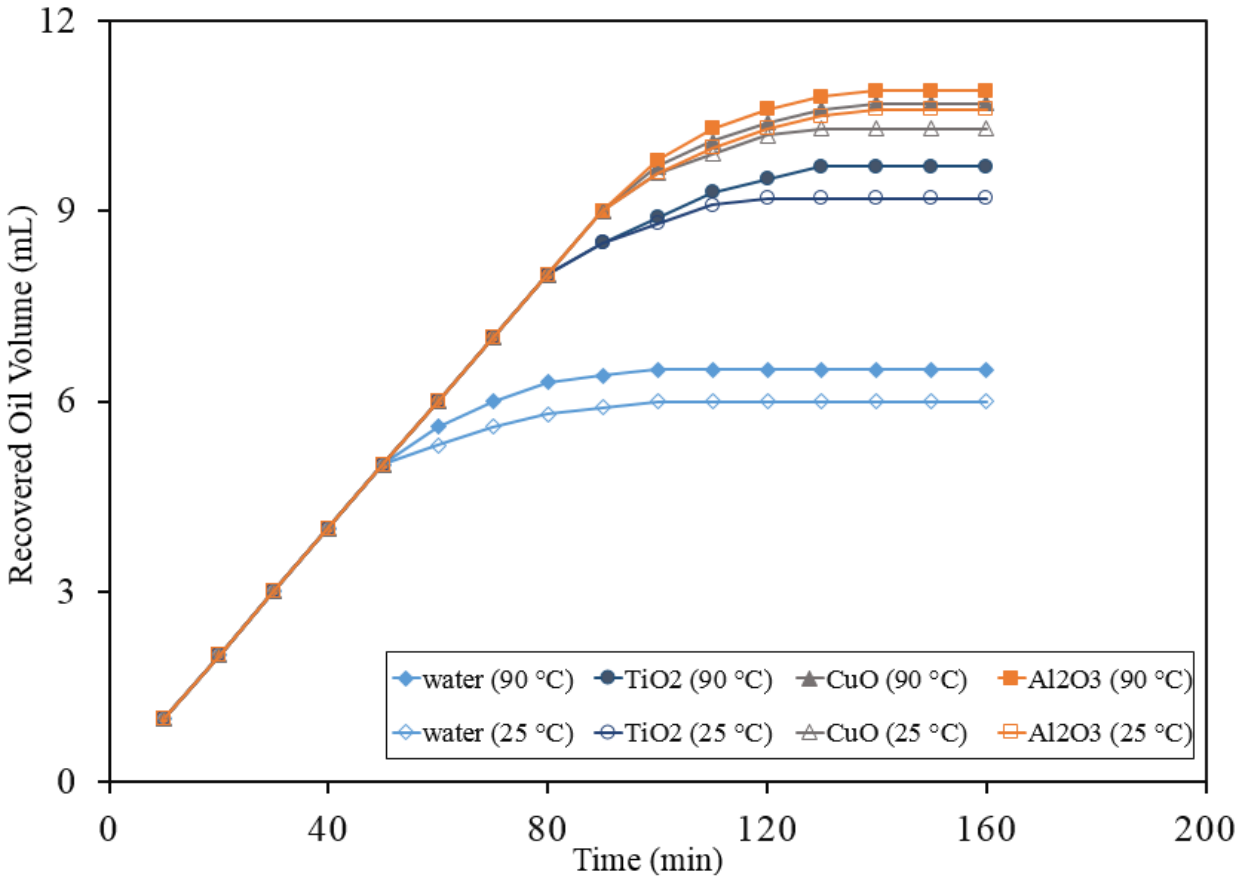

Figure 16: Recovered oil volume during the time when water/nanofluid is injected at different temperatures with flowrate of 0.1 mL/min in antigravity direction.

Table 7: Volume of recovered oil when injecting fluids at different temperatures.

Type of fluid	Temperature(°C)	Recovered Oil Volume(mL)	Error rate caused by 3 repetitions of experiments (%)
Pure water	25	6	<1
	90	6.5	≈1
TiO_2	25	9.2	<1
	90	9.7	<1
CuO	25	10.3	<0.5
	90	10.7	≈0.5
γ-Al_2O_3	25	10.6	<0.5
	90	10.9	<0.5

Figure (17) shows the maximum volume of the recovered oil when water/nanofluids are injected at two different temperatures. As discussed, for oil-water and oil-TiO_2 nanofluid displacements the maximum effect on the oil recovery were predicted.

This is due to the less impact of the temperature change on the oil-water and oil-TiO_2 interfacial tension.

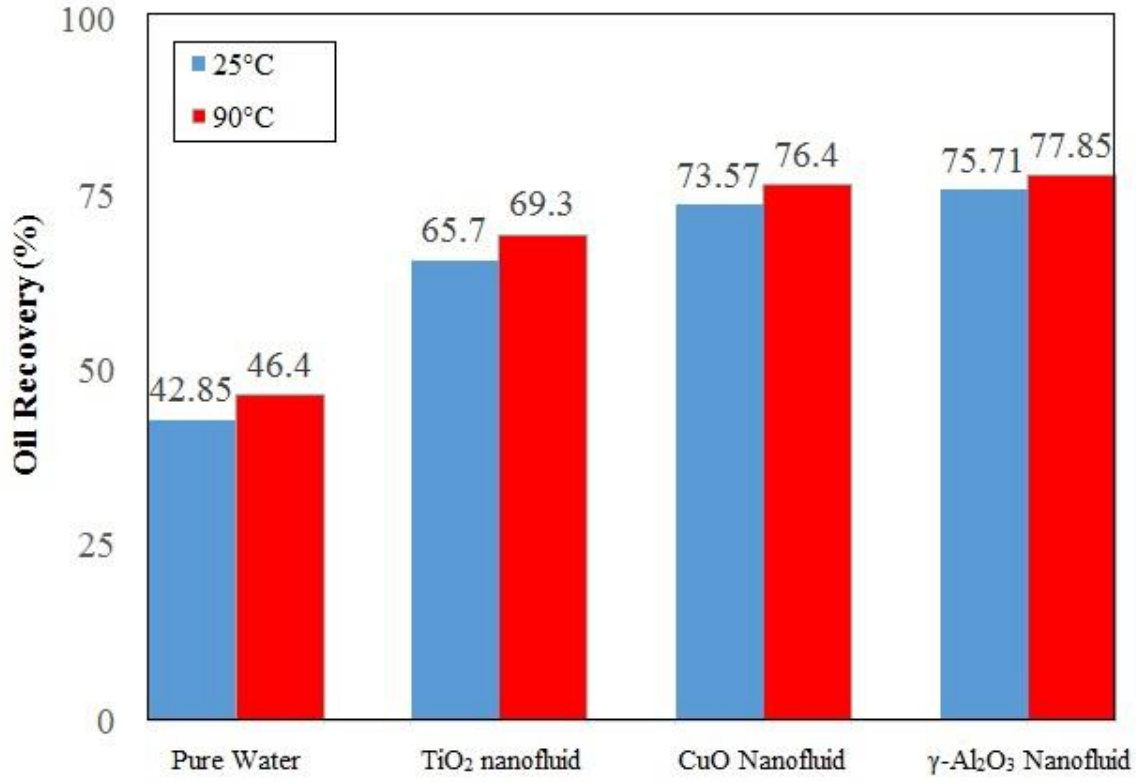

Figure 17: The maximum oil recovery by injecting water/nanofluids in antigravity direction with a flowrate of 0.1 mL/min at 25 °C and 90 °C.

4. Conclusion

In the present experimental study, effects of temperature and nanofluid type on the oil recovery from a vertical porous media during antigravity and gravity-aligned fluid injection were investigated. The pure water injection into the double-walled reservoir at different flowrates showed that the oil recovery increases with decreasing flowrate from 0.4 to 0.1 mL/min due to increasing in injected fluid resident time. Thus, 0.1 mL/min was selected at the optimum flowrate. To investigate the impact of fluid injection direction on the oil recovery, results of the antigravity fluid injection was compared to the gravity-aligned fluid injection results. Results proved that due to the higher density of injected fluids compared to

the base oil's and effects of weight force led to stability in fluid-fluid interfacial morphology and enhanced oil recovery. In gravity-aligned direction fluid injection, Rayleigh–Taylor instability reduces the recovery of oil. To explore the effects of nanofluids type on oil recovery, TiO_2, γ-Al_2O_3, and CuO nanoparticles at various concentrations with surfactant (SDS and Xanthan gum) at critical micelle concentration were used. The findings demonstrated that as nanoparticle concentration increases, the volume of the recovered oil also increases as well. Eventually, nanofluids with 1 %wt nanoparticles concentration were selected for rest of the experimentation. Considering the high density and the hydrophilicity of γ-Al_2O_3 nanofluid, the oil recovery by injecting Al_2O_3 nanofluid was better than the others. Note that, the oil recovery was also enhanced by injecting TiO_2 and CuO nanofluids compared to the pure water due to the significant reduction in the interfacial tension. Also, injecting hot fluids (with a temperature of 90 °C) indicated a slight enhancement in oil recovery. Eventually, with injecting hot pure water, TiO_2, CuO, and Al_2O_3 nanofluids in antigravity direction at constant flowrate of 0.1 ml/min, oil recovery reached to 46.4, 69.3, 76.4, and 77.85%, respectively. Overall, injection of Al_2O_3 nanofluid in antigravity direction without considering the effect of temperature led to the ideal and most advantageous result in the current research, which enhanced the efficiency of oil recovery to 75.1 and 77.85% at 25 °C and 90 °C, respectively.

Declarations

- The authors declare that they have no known competing financial interests or personal relationships that could have appeared to influence the work reported in this paper.
- All authors have participated in conception, analysis and interpretation of the data, drafting the article and revising it, and approval of the final version.
- This manuscript has not been submitted to, nor is under review at, another journal or other publishing venue.
- Results of the study have been presented clearly, honestly, and without fabrication and data manipulation.
- Proper acknowledgements to other works have been given.

References

[1] Ahmadlouydarab, M., Ghaffari, K. and Jafari, A. 2021. "*Effects of Phase Change on Enhanced Oil Recovery During Injection of Steam Carrying Alumina Nanoparticles: Numerical Simulation*", Arab J Sci Eng. https://doi.org/10.1007/s13369-021-05738-w

[2] Lim, M., Pope, G. and Sepehrnoori, K. 1994. "*Mechanistic study of carbon dioxide flooding using horizontal wells*", SPE. https://doi.org/10.2118/27807-MS

[3] Morris, J. P., Hao, Y., Foxall, W. and McNab, W. 2011. "*A study of injection-induced mechanical deformation at the In Salah CO_2 storage project*", International Journal of Greenhouse Gas Control, 5(2), pp. 270-280. https://doi.org/10.1016/j.ijggc.2010.10.004

[4] Mai, A., Bryan, J., Goodarzi, N. and Kantzas, A. 2009. "*Insights Into Non-Thermal Recovery of Heavy Oil*", J Can Pet Technol, 48(3), pp. 27-35. https://doi.org/10.2118/09-03-27

[5] Nair, R. R., Protasova, E. and Bilstad, T. 2016. "*Smart Water for Enhanced Oil Recovery by Nano-Filtration*", Journal of Petroleum & Environmental Biotechnology, 7(2). http://dx.doi.org/10.4172/2157-7463.1000273

[6] Stosur, G. 2003. "*EOR: Past, present and what the next 25 years may bring*", SPE. https://doi.org/10.2118/84864-MS

[7] Pei, X., Zhai, K., Liang, X., Deng, Y., Tan, Y., Wang, P. and Xu, K. 2017. "*Interfacial Activity of Starch-Based Nanoparticles at the Oil-Water Interface*", Langmuir, 33(15), pp. 3787-3793. https://doi.org/10.1021/acs.langmuir.7b00035

[8] Karimi, A., Fakhroueian, Z., Bahramian, A., Pour Khiabani, N., Babaee Darabad, J., Azin, R. and Arya, S. 2012. "*Wettability Alteration in Carbonates using Zirconium Oxide Nanofluids: EOR Implications*", Energy Fuels, 26(2), pp. 1028-1036. https://doi.org/10.1021/ef201475u

[9] Deng, X., Shahzad-Kamal, M., Patil, S., Shakil-Hussain, S. M. and Zhou, X. 2020. "*A Review on Wettability Alteration in Carbonate Rocks: Wettability Modifiers*", Energy Fuels, 34(1), pp. 31-54. https://doi.org/10.1021/acs.energyfuels.9b03409

[10] Luo, D., Wang, F., Zhu, J., Cao, F., Liu, Y. and Li, X. 2016. "*Nanofluid of graphene-based amphiphilic Janus nanosheets for tertiary or enhanced oil recovery: High performance at low concentration*", Proceedings of the National Academy of Sciences of the United States of America, 113(28), pp. 7711-7716. https://doi.org/10.1073/pnas.1608135113

[11] Monfared, A. D., Ghazanfari, M. H., Jamialahmadi, M. and Helalizadeh, A. 2016. "*Potential Application of Silica Nanoparticles for Wettability Alteration of Oil–Wet Calcite: A Mechanistic Study*", Energy Fuels, 30(5), pp. 3947-3961. https://doi.org/10.1021/acs.energyfuels.6b00477

[12] Mousavi-Moghadam, A. and Baghban-Salehi, M. 2019. "*Enhancing hydrocarbon productivity via wettability alteration: A review on the application of nanoparticles*", Reviews in Chemical Engineering, 35(6). https://doi.org/10.1515/revce-2017-0105

[13] Lim, S., Horiuchi, H., Nikolov, A. D. and Wasan, D. 2015. "*Nanofluids Alter the Surface Wettability of Solids*", Langmuir, 31(21), pp. 5827-5835. https://doi.org/10.1021/acs.langmuir.5b00799

[14] Hu, Z., Haruna, M., Gao, H., Nourafkan, E. and Wen, D. 2017. "*Rheological Properties of Partially Hydrolyzed Polyacrylamide Seeded by Nanoparticles*", Ind. Eng. Chem. Res, 56(12), pp. 3456–3463. https://doi.org/10.1021/acs.iecr.6b05036

[15] Choi, S. K., Son, H. A., Kim, H. T. and Kim, J. W. 2017. "*Nanofluid Enhanced Oil Recovery Using Hydrophobically Associative Zwitterionic Polymer-Coated Silica Nanoparticles*", Energy Fuels, 31(8), pp. 7777-7782. https://doi.org/10.1021/acs.energyfuels.7b00455

[16] Hu, Z., Azmi, S. M., Raza, G., Glover, P. W. J. and Wen, D. 2016. "*Nanoparticle-Assisted Water-Flooding in Berea Sandstones*", Energy Fuels, 30(4), pp. 2791-2804. https://doi.org/10.1021/acs.energyfuels.6b00051

[17] Chegenizadeh, N., Saeedi, A. and Quan, X. 2016. "*Application of nanotechnology for enhancing oil recovery – A review*", Petroleum, 2(4), pp. 324-333. https://doi.org/10.1016/j.petlm.2016.10.002

[18] Hamouda, A. A. and Gomari, K. A. R. 2006. "*Influence of Temperature on Wettability Alteration of Carbonate Reservoirs*", SPE. https://doi.org/10.2118/99848-MS

[19] Suleimanov, B. A., Ismailov, F. S. and Veliyev, E. F. 2011. "*Nanofluid for enhanced oil recovery*", Journal of Petroleum Science and Engineering, 78(2), pp. 431-437. https://doi.org/10.1016/j.petrol.2011.06.014

[20] Maghzi, A., Kharat, R., Mohebbi, A. and Ghazanfari, M. H. 2014. "*The impact of silica nanoparticles on the performance of polymer solution in presence of salts in polymer flooding for heavy oil recovery*", Fuel, 123, pp. 123-132. https://doi.org/10.1016/j.fuel.2014.01.017

[21] Maghzi, A., Kharat, R., Mohebbi, A. and Ghazanfari, M. H. 2011. "*Pore-Scale Monitoring of Wettability Alteration by Silica Nanoparticles During Polymer Flooding to Heavy Oil in a Five-Spot Glass Micromodel*", Transport in Porous Media, 87, pp. 653-664. https://doi.org/10.1007/s11242-010-9696-3

[22] El-Diasty, A. I. and Aly, A. M. 2015. "*Understanding the Mechanism of Nanoparticles Applications in Enhanced Oil Recovery*", SPE. https://doi.org/10.2118/175806-MS

[23] Yousefvand, H. and Jafari, A. 2015. "*Enhanced Oil Recovery Using Polymer/nanosilica*", Procedia Materials Science, 11, pp. 565-570. https://doi.org/10.1016/j.mspro.2015.11.068

[24] Roustaei, A. and Bagherzadeh, H. 2015. "*Experimental investigation of SiO_2 nanoparticles on enhanced oil recovery of carbonate reservoirs*", J Petrol Explor Prod Technol, 5, pp. 27-33. https://doi.org/10.1007/s13202-014-0120-3

[25] Wang, Sh., Chen, Ch., Shiau, B. J. and Harwell, J. H. 2017. "*Enhancing foam stability in porous media by applying nanoparticles*", Journal of Dispersion Science and Technology, 39(5), pp. 734-743. https://doi.org/10.1080/01932691.2017.1388175

[26] Soleimani, H., Khurram-Baig, M., Yahya, N., Khodapanah, L., Sabet, M., Demiral, B. M. R. and Burda, M. 2018. "*Synthesis of ZnO nanoparticles for oil–water interfacial tension reduction in enhanced oil recovery*", Applied Physics A. https://doi.org/10.1007/s00339-017-1510-4

[27] Mahmoudi, S., Jafari, A. and Javadian, S. 2019. "*Temperature effect on performance of nanoparticle/surfactant flooding in enhanced heavy oil recovery*", Pet. Sci, 16, pp. 1387–1402. https://doi.org/10.1007/s12182-019-00364-6

[28] Deng, X., Tariq, Z., Murtaza, M., Patil, S., Mahmoud, M. and Kamal, M. S. 2021. "*Relative contribution of wettability Alteration and interfacial tension reduction in EOR: A critical review*", Journal of Molecular Liquids, 325, pp. 115175. https://doi.org/10.1016/j.molliq.2020.115175

[29] Chandio, T. A., Manan, M. A., Memon, K. R., Abbas, G. and Abbasi, G. R. 2021. "*Enhanced Oil Recovery by Hydrophilic Silica Nanofluid: Experimental Evaluation of the Impact of Parameters and Mechanisms on Recovery Potential*", Energies, 14(18), pp. 5767. https://doi.org/10.3390/en14185767

[30] Cao, J., Chen, Y., Zhang, J., Wang, X., Wang, J., Shi, C., Ning, Y. and Wang, X. 2022. "*Preparation and application of nanofluid flooding based on polyoxyethylated graphene oxide nanosheets for enhanced oil recovery*", Chemical Engineering Science, 247, pp. 117023. https://doi.org/10.1016/j.ces.2021.117023

[31] Sawhney, G. S., Liebe, H. and Butler, R. M. 1995. "*Vertical Injection Wells For Sagd: A Practical Option Or Not?*", Journal of Canadian Petroleum Technology, 34(01), pp. 95-01-06. https://doi.org/10.2118/95-01-06

[32] Liu, S., Agarwal, R., Sun, B., Wang, B., Li, H., Xu, J. and Fu, G. 2021. "*Numerical simulation and optimization of injection rates and wells placement for carbon dioxide enhanced gas recovery using a genetic algorithm*", Journal of Cleaner Production, 280(2), pp. 124512. https://doi.org/10.1016/j.jclepro.2020.124512

[33] Dong, M. and Huang, S. 2002. "*Flue Gas Injection for Heavy Oil Recovery*", Journal of Canadian Petroleum Technology, 41(09). https://doi.org/10.2118/02-09-04

[34] Joshi, S. D. 1986. "*A Laboratory Study of Thermal Oil Recovery Using Horizontal Wells*", SPE Enhanced Oil Recovery Symposium. https://doi.org/10.2118/14916-MS

[35] Shen, P., Wang, J., Yuan, S., Zhong, T. and Jia, X. 2009. "*Study of Enhanced-Oil-Recovery Mechanism of Alkali/Surfactant/Polymer Flooding in Porous Media From Experiments*", SPE Journal, 14(02), pp. 237–244. https://doi.org/10.2118/126128-PA

[36] Bhaisare, M. L., Pandey, S., Khan, M. S., Talib, A. and Wu, H. F. 2015. "*Fluorophotometric determination of critical micelle concentration (CMC) of ionic and non-ionic surfactants with carbon dots via Stokes shift*", Talanta, 132, pp. 572-578. https://doi.org/10.1016/j.talanta.2014.09.011

[37] Saha, R., Uppaluri, R. V. S. and Tiwari, P. 2019. "*Impact of Natural Surfactant (Reetha), Polymer (Xanthan Gum), and Silica Nanoparticles To Enhance Heavy Crude Oil Recovery*", Energy Fuels, 33(5), pp. 4225–4236. https://doi.org/10.1021/acs.energyfuels.9b00790

[38] Keykhosravi, A., Bagheri Vanani, M. and Aghayari, C. 2021. "*TiO_2 nanoparticle-induced Xanthan Gum Polymer for EOR: Assessing the underlying mechanisms in oil-wet carbonates*", Journal of Petroleum Science and Engineering, 204, pp. 108756. https://doi.org/10.1016/j.petrol.2021.108756

[39] Gbadamosi, A., Yusuff, A., Agi, A., Muruga, P., Junin, R. and Jeffrey, O. 2022. "*Mechanistic study of nanoparticles-assisted xanthan gum polymer flooding for enhanced oil recovery: a comparative study*", J Petrol Explor Prod Technol, 12, pp. 207–213. https://doi.org/10.1007/s13202-021-01334-8

[40] Gooch, J. W. 2007. "*Encyclopedic Dictionary of Polymers*", pp. 318, ISBN 978-1-4419-6246-1.

[41] Clogston, J. D. and Patri, A. k. 2011. "*Zeta Potential Measurement*", Characterization of Nanoparticles Intended for Drug Delivery, 697, pp. 63-70. https://doi.org/10.1007/978-1-60327-198-1_6

[42] Praveen, P., Viruthagiri, G., Mugundan, S. and Shanmugam, N. 2014. "*Structural, optical and morphological analyses of pristine titanium di-oxide nanoparticles – Synthesized via sol–gel route*", Spectrochimica Acta Part A: Molecular and Biomolecular Spectroscopy, 117, pp. 622-629. https://doi.org/10.1016/j.saa.2013.09.037

[43] Jnido, G., Ohms, G. and Viöl, W. 2019. "*Deposition of TiO_2 Thin Films on Wood Substrate by an Air Atmospheric Pressure Plasma Jet*", Coatings, 9(7), pp. 441. https://doi.org/10.3390/coatings9070441

[44] Bodade, A. B., Taiwade, M. A. and Chaudhari, G. N. 2017. "*Bioelectrode based chitosan-nano copper oxide for application to lipase biosensor*", Journal of Applied Pharmaceutical Research, 5(1), pp. 30-39.

[45] Arun, K. J., Batra, A. K., Krishna, A., Bhat, K., Aggarwal, M. D. and Francis, P. J. J. 2015. "*Surfactant Free Hydrothermal Synthesis of Copper Oxide Nanoparticles*", American Journal of Materials Science, 5(3A), pp. 36-38. doi:10.5923/s.materials.201502.06

[46] Ethiraj, A. S. and Kang, D. J. 2012. "*Synthesis and characterization of CuO nanowires by a simple wet chemical method*", Nanoscale Res Lett, 7. https://doi.org/10.1186/1556-276X-7-70

[47] Khodadadi, A., Farahmandjou, M. and Yaghoubi, M. 2019. "*Investigation on synthesis and characterization of Fe-doped Al_2O_3 nanocrystals by new sol–gel precursors*", Mater. Res. Express, 6(2), pp. 025029. https://doi.org/10.1088/2053-1591/aaef70

[48] Toledo, R. R., Santoyo, V. R. and Sánchez, D. M. 2018. "*Effect of aluminum precursor on physicochemical properties of Al_2O_3 by hydrolysis/precipitation method*", Nova scientia, 10(20). https://doi.org/10.21640/ns.v10i20.1217

[49] Abdollahifar, M., Zamani, R., Beiygie, E. and Nekouei, H. 2014. "*Synthesis of micro-mesopores flowerlike γ-Al_2O_3 nano-architectures*", Journal of the Serbian Chemical Society, 79(8), pp. 1007-1017. https://doi.org/10.2298/JSC130903007A

[50] Wen, W., Hai, J., Yao, J., Gu, Y.-J., Kobayashi, H., Tian, H., Sun, T., Chen, Q., Yang, P., Geng, C. and Wu, J.-M. 2021. "*Univariate Lattice Parameter Modulation of Single-Crystal-like Anatase TiO_2 Hierarchical Nanowire Arrays to Improve Photoactivity*", Chem. Mater, 33(4), pp. 1489–1497. https://doi.org/10.1021/acs.chemmater.1c00089

[51] Tonejc, A. M., Djerdj, I. and Tonejc, A. 2002. "*An analysis of evolution of grain size-lattice parameters dependence in nanocrystalline TiO_2 anatase*", Materials Science and Engineering: C, 19(1-2), pp. 85-89. https://doi.org/10.1016/S0928-4931(01)00447-7

[52] Wang, J., Zhou, T., Zhang, Y., Chen, S., Bai, J., Li, J., Zhu, H. and Zhou, B. 2021. "*The design of high performance photoanode of CQDs/TiO_2/WO_3 based on DFT alignment of lattice parameter and energy band, and charge distribution*", Journal of Colloid and Interface Science, 600, pp. 828-837. https://doi.org/10.1016/j.jcis.2021.05.086

[53] Dhanasekaran, V., Soundaram, N., Kim, S.-I., Chandramohan, R., Mantha, S., Saravanakumar, S. and Mahalingam, T. 2014. "*Optical, electrical and microstructural studies of monoclinic CuO nanostructures synthesized by a sol–gel route*", New J. Chem, 38(6), pp. 2327–2333. https://doi.org/10.1039/C4NJ00084F

[54] Cao, H., Zhou, Z., Yu, J. and Zhou, X. 2018. "*DFT study on structural, electronic, and optical properties of cubic and monoclinic CuO*", J Comput Electron, 17, pp. 21–28. https://doi.org/10.1007/s10825-017-1057-9

[55] Liang, J., Chen, Z., Wu, F. and Xie, S. 1990. "*Phase diagram of SrO-CaO-CuO ternary system*", Solid State Communications, 75(3), pp. 247-252. https://doi.org/10.1016/0038-1098(90)90279-K

[56] Samain, L., Jaworski, A., Edén, M., Ladd, D. M., Seo, D.-K., Javier Garcia-Garcia, F. and Häussermann, U. 2014. "*Structural analysis of highly porous γ-Al_2O_3*", Journal of Solid State Chemistry, 217, pp. 1-8. https://doi.org/10.1016/j.jssc.2014.05.004

[57] Tekeli, S. 2007. "*The solid solubility limit of Al_2O_3 and its effect on densification and microstructural evolution in cubic-zirconia used as an electrolyte for solid oxide fuel cell*", Materials & Design, 28(2), pp. 713-716. https://doi.org/10.1016/j.matdes.2005.09.011

[58] Helmy, E. T., El Nemr, A., Mousa, M., Arafa, E. and Eldafrawy, S. 2018. "*Photocatalytic degradation of organic dyes pollutants in the industrial textile wastewater by using synthesized TiO_2, C-doped TiO_2, S-doped TiO_2 and C,S co-doped TiO_2 nanoparticles*", J Water Environ Nanotechnol, 3(2), pp. 116-127. https://dx.doi.org/10.22090/jwent.2018.02.003

[59] Haider, A. J., AL– Anbari, R. H., Kadhim, G. R. and Salame, C.T. 2017. "*Exploring potential Environmental applications of TiO_2 Nanoparticles*", Energy Procedia, 119, pp. 332-345. https://doi.org/10.1016/j.egypro.2017.07.117

[60] Dzhardimalieva, G. I. and Uflyand, I.E. 2017. "*Design and synthesis of coordination polymers with chelated units and their application in nanomaterials science*", RSC Adv, 7, pp. 42242-42288. https://doi.org/10.1039/C7RA05302A

[61] Koltsov, I., Smalc-Koziorowska, J., Prześniak-Welenc, M., Małysa, M., Kimmel, G., McGlynn, J., Ganin, A. and Stelmakh, S. 2018. "*Mechanism of Reduced Sintering Temperature of Al_2O_3–ZrO_2 Nanocomposites Obtained by Microwave Hydrothermal Synthesis*", Materials, 11(5), pp. 829. https://doi.org/10.3390/ma11050829

[62] Sagar, T. V., Rao, T. S. and Raghuram, N. 2020. "*Temperature dependent structural, morphological, FTIR, optical, magnetic properties of NiMgZn ferrites*", Nanosystems: Phys. Chem. Math, 11(4), pp. 434–443. https://doi.org/10.17586/2220-8054-2020-11-4-434-443

[63] Rostami, S., Ahmadlouydarab, M. and Sharifi-Haddad, A. 2022. "*Effects of hot nanofluid injection on oil recovery from a model porous medium*", Chemical Engineering Research and Design, 186, pp. 451-461. https://doi.org/10.1016/j.cherd.2022.08.013

[64] Shi, Z., Zhang, Y., Liu, M., Hanaor, D. A. H. and Gan, Y. 2018. "*Dynamic contact angle hysteresis in liquid bridges*", Colloids and Surfaces A: Physicochemical and Engineering Aspects, 555, pp. 365-371. https://doi.org/10.1016/j.colsurfa.2018.07.004

[65] Sharp, D. H. 1984. "*An overview of Rayleigh-Taylor instability*", Physica D, 12(1), pp. 3-18. https://doi.org/10.1016%2F0167-2789%2884%2990510-4

[66] Günther, A. and Jensen, K. F. 2006. "*Multiphase microfluidics: from flow characteristics to chemical and materials synthesis*", Lab Chip, 6(12), pp. 1487–1503. https://doi.org/10.1039/B609851G

[67] Greiner, W., Müller, B. and Rafelski, J. 1985. "*The Hole Theory*". In: Quantum Electrodynamics of Strong Fields. Texts and Monographs in Physics. Springer, Berlin, Heidelberg. https://doi.org/10.1007/978-3-642-82272-8_4